Akshay Pujari[1]
Department of Mechanical and Industrial Engineering,
University of Massachusetts,
Amherst, MA 01003

Alexander F. Smith[1]
Department of Mechanical and Industrial Engineering,
University of Massachusetts,
Amherst, MA 01003

Joshua D. Hall
Department of Mechanical and Industrial Engineering,
University of Massachusetts,
Amherst, MA 01003

Patrick Mei
Department of Biochemistry and Molecular Biology,
University of Massachusetts,
Amherst, MA 01003

Kin Chau
Department of Mechanical and Industrial Engineering,
University of Massachusetts,
Amherst, MA 01003

Duy T. Nguyen
Department of Mechanical and Industrial Engineering,
University of Massachusetts,
Amherst, MA 01003

Daniel T. Sweet
Department of Medicine and Division of Cardiology,
University of Pennsylvania,
Philadelphia, PA 19104

Juan M. Jiménez[2]
Department of Mechanical and Industrial Engineering,
University of Massachusetts,
N575 Life Sciences Laboratory,
240 Thatcher Way Amherst
Amherst, MA 01003;
Department of Biomedical Engineering,
University of Massachusetts,
Amherst, MA 01003
e-mail: juanjimenez@umass.edu

Lymphatic Valves Separate Lymph Flow Into a Central Stream and a Slow-Moving Peri-Valvular Milieu

The lymphatic system plays a pivotal role in the transport of fats, waste, and immune cells, while also serving as a metastatic route for select cancers. Using live imaging and particle tracking, we experimentally characterized the lymph flow field distal from the inguinal lymph node in the vicinity of normal bileaflet and malformed unileaflet intraluminal valves. Particle tracking experiments demonstrated that intraluminal lymphatic valves concentrate higher velocity lymph flow in the center of the vessel, while generating adjacent perivalvular recirculation zones. The recirculation zones are characterized by extended particle residence times and low wall shear stress (WSS) magnitudes in comparison to the rest of the lymphangion. A malformed unileaflet valve skewed lymph flow toward the endothelium on the vessel wall, generating a stagnation point and a much larger recirculation zone on the opposite wall. These studies define physical consequences of bileaflet and unileaflet intraluminal lymphatic valves that affect lymph transport and the generation of a heterogeneous flow field that affects the lymphatic endothelium nonuniformly. The characterized flow fields were recreated in vitro connecting different flow environments present in the lymphangion to a lymphatic endothelial cell (LEC) pro-inflammatory phenotype. Unique and detailed insight into lymphatic flow is provided, with potential applications to a variety of diseases that affect lymph transport and drug delivery. [DOI: 10.1115/1.4048028]

Keywords: lymph, lymph flow, lymphangion, lymphatics, wall shear stress, valve, malformed valve

Introduction

The transport of lymph throughout the lymphatic system is an incompletely understood process and can vary significantly from one species to another [1]. Interstitial fluid is taken up by the initial lymphatics, removing cell waste and toxins from the interstitial space. The uptake of fluid, macromolecules, and lymphocytes is aided by flap-like mini-valves formed by overlapping endothelial cells (ECs), aquaporin-1 water channels, and highly permeable button-like junctions in the initial lymphatics [2–5]. The initial lymphatics lack a basement membrane and are composed of a monolayer of lymphatic endothelial cells (LECs) with long cytoplasmic projections anchored to surrounding connective tissue [6,7]. The initial lymphatics drain into precollector and subsequently collector lymphatic vessels, with an increase in lumen size. The number of initial lymphatics draining into precollector lymphatic vessels varies by organ. The precollector and collector lymphatic vessels are distinguished by the presence of intraluminal valves. However, collectors also exhibit smooth muscle cell layers to aid in the pumping of lymph. Ex vivo and computational

[1]These authors contributed equally to this work.
[2]Corresponding author.
Manuscript received January 7, 2020; final manuscript received July 28, 2020; published online August 31, 2020. Assoc. Editor: David Corr.

experiments have demonstrated that, following smooth muscle cell contraction, lymphatic vessels distend when externally tethered or with positive transmural pressure [8]. This vessel dilation creates a suction force that propagates to precollector lymphatics enhancing uptake of interstitial fluid from tissues, even at subatmospheric pressures [8]. Overall, lymph is transported via a series of lymphatic vessels that progressively become less permeable, utilizing valves to yield net antegrade flow.

Lymph is propelled through the lymphatic vessel network by transient pressure gradients in conjunction with intraluminal lymphatic valves, lymphatic vessel contraction, and local tissue motion. In the absence of a central pumping organ like the heart, pumping of lymph is highly decentralized with local motion driving the flow, and is subject to intra- and interanimal variation. Although physiologically normal, out-of-sequence contractions of neighboring lymphangions and incomplete closure of intraluminal valves may decrease net antegrade lymph flow and cause local retrograde lymph flow, even in the absence of disease. While it has been observed in unaffected individuals, lymph retrograde flow is more commonly associated with patients suffering from lymphedema [9]. Retrograde lymph flow due to lymphedema is associated with significantly dilated lymphatic vessels, which render valves insufficient. Lymph flow in both directions is commonly observed in dilated lymphatic vessels. The importance of bidirectional lymph flow and its effects on lymphatic homeostasis are largely unknown [1].

While the directionality of lymph transport may be relevant in cancer metastasis, lymphedema, immunity, and homeostasis, the mechanisms that regulate lymph transport are incompletely understood. One of the mechanisms to propel lymph forward in collector vessels is phasic contractions of lymphangions by the smooth muscle cells in the tunica media [10,11]. In the study by Dixon et al., even though the frequency and amplitude of contractions were heterogenous between various mesenteric lymphatic vessels, the relationship between vessel contraction and fluid velocity remained relatively consistent [12]. Phasic contractility parameters, including amplitude and frequency, have been quantified in vivo using near-infrared tracer imaging and have been suggested to be dependent on wall shear stress (WSS) [12,13]. Although difficult to directly measure, the average lymphatic WSS has been estimated to be 0.64 ± 0.14 dyn/cm^2 in rat mesenteric lymphatic vessels using lymphocyte velocity and vessel diameter measurements [12].

Akin to ECs in the blood circulatory system, LECs respond to WSS stimuli by upregulation and downregulation of a variety of genes. WSS has been shown to regulate lymphatic endothelial permeability in an inversely proportional manner where greater WSS magnitudes elicit lower permeability. This WSS effect can be abrogated via inhibition of RAC-1 [14]. in vivo, inducible deletion of the transcription factor Forkhead-box protein C2 (FOXC2) confers abnormal shear stress sensing by LECs resulting in cell–cell junction defects, regression of lymphatic valves, and lymphatic vessel collapse, leading to lymphatic dysfunction and lethality [15]. C-type lectin-like receptor 2 (CLEC2) deficient mice experience disruption of lymph flow during development leading to lack of WSS stimuli on LECs and failed development of lymphatic valves; this phenotype is also observed with lack of FOXC2 [16]. In contrast, exposing LECs to WSS in vitro upregulated the expression of GATA-binding factor 2 (GATA2) and FOXC2, genes involved in lymphatic valve development, in

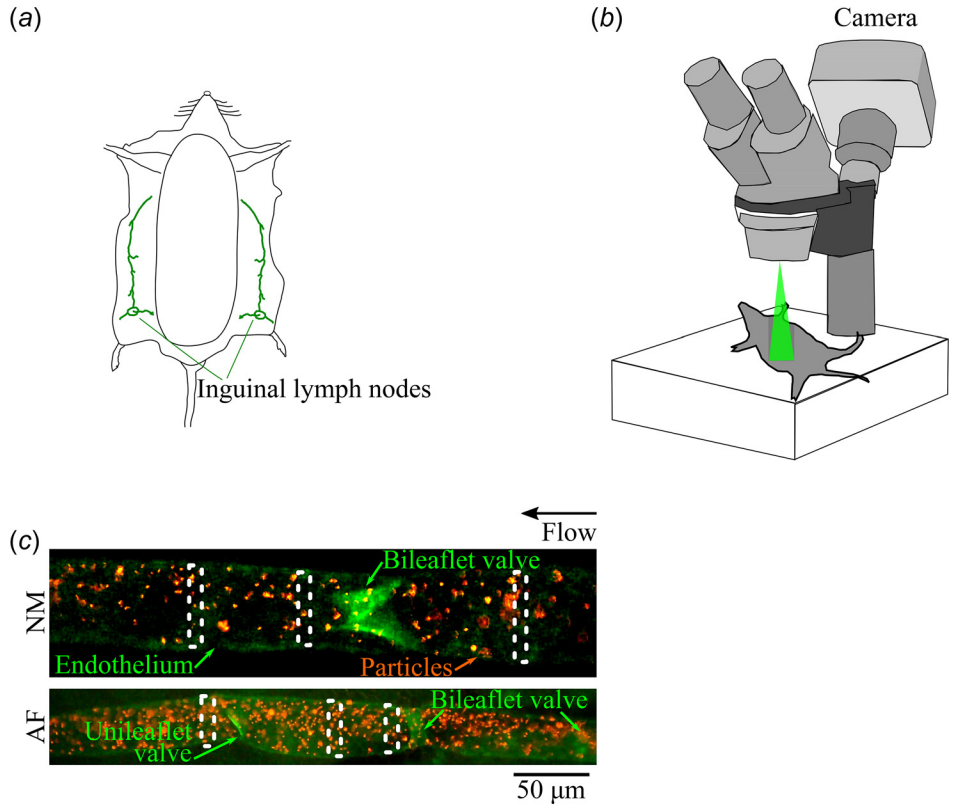

Fig. 1 (*a*) A schematic of the mouse model highlights the ROI distal from the inguinal lymph node, (*b*) which was imaged using a dissecting epifluorescence microscope. (*c*) The regions of interest are shown for both the normal (NM) and affected (AF) mice. The normal mouse ROI has one intraluminal bileaflet valve, while the affected mouse has one intraluminal unileaflet valve (left) and two intraluminal bileaflet valves (center and right). White-dashed rectangles denote segments where the flow and wall movements were further analyzed. The direction of lymph flows from right to left.

comparison to LECs in static conditions, which simulates the lack of lymph flow experienced by LECs in CLEC2 deficient mice [16].

In the circulatory system, WSS stimuli promote either an anti-inflammatory or pro-inflammatory endothelial gene and protein expression environment that regulates transmigration of leukocytes. For example, arterial ECs exposed to atherosusceptible WSS waveforms shift to a pro-inflammatory phenotype characterized by upregulation of inflammatory cytokines, leukocyte attracting chemokines, and surface adhesion molecules that mediate cellular adhesion and extravasation [17–19]. Various chemokines (IL-8, CCL2, and CXCL2) as well as cellular adhesion molecules (ICAM-1, ICAM-2, JAM-A, and LYVE-1) are known mediators of endothelial transmigration of leukocytes in the blood circulatory system. Akin to the circulatory system, the process of leukocyte migration in the lymphatic system is triggered by an inflammatory response [20]. The lymphatic system is actively involved in the initiation and resolution of inflammation, with lymphatic vessels serving as a route for lymphocytes and newly activated dendritic cells to lymph nodes, and plays an important role in leukocyte extravasation from tissues during resolution of inflammation [21]. However, the role of lymphatic flow in the inflammatory response of LECs has not been thoroughly examined.

In order to elucidate the effects of WSS on lymphatic mechanobiology, it is crucial to characterize the fluid flow environment that dictates fluid forces. To address this need, to the best of our knowledge, the work presented herein is the first time that the lymph flow field distal from the inguinal lymph node has been characterized in vivo. In addition, the lymph flow field was recreated in vitro to demonstrate a WSS-dependent pro-inflammatory LEC phenotypic change. in vivo characterization of lymphatic flow is important to understanding a variety of diseases with affected lymph flow, and normal drug transport in the lymphatic system. Herein, we experimentally examined how lymph transport is affected by intraluminal malformed unileaflet and normal bileaflet valves in vivo. Results from particle tracking and wall contractility measurements in lymphatic vessels of mice are presented along with in vitro LEC gene and protein WSS-dependent expression.

Materials and Methods

All animal experiments were approved by the University of Pennsylvania Institutional Animal Care and Use Committee. Prox1-GFP BAC transgenic mice obtained from the Mutant Mouse Regional Resource Centers (MMRRC) were used for the experiments [22]. Two 4-week-old mice weighing between 18 and 20 g were selected for the studies due to enhanced visibility of lymphatic vessels, since optical clarity of lymphatic vessels is compromised in older mice due to greater deposition of adipose tissue. One mouse had normally formed bileaflet valves and is referred to as the normal mouse. The field of view of the other mouse had two normal bileaflet valves and one congenital abnormal unileaflet valve, and is referred to as the affected mouse. The term affected is used only as a label to differentiate the mice in regard to this focal congenital valve defect, and in no way to imply the presence of disease. Mice were anesthetized using 2,2,2-tribromoethanol (Sigma-Aldrich, St. Louis, MO) dissolved in tert-amyl alcohol (Sigma-Aldrich) (0.5 mg/g). Supplemental doses of the anesthetic were administered as necessary. Body temperature was maintained at 37 °C via an animal temperature controller and warming pad (ATC2000, World Precision Instruments, Sarasota, FL). A thoracic incision allowed peeling back of ventral skin and inguinal lymph node exposure (Fig. 1(*a*)). Five microliters of 1 μm polyethylene glycolylated FluoSpheres latex particles (Thermo Fisher Scientific, Inc., 580/605, Waltham, MA) were injected with a 32-gauge needle at a concentration of 1×10^8 beads/mL into the inguinal lymph node. The small volume of particles injected is insignificant in comparison to the volume of the lymph node to ensure that the flow is not affected. Particle images were collected about 30 s after injection to avoid any potential disturbance introduced by the injection of particles. Particle displacement through efferent lymphatic vessels was imaged with an Olympus MVX10 dissecting microscope and recorded with a Nikon D5200 camera at a rate of 29.97 frames per second (Fig. 1(*b*)). Particle displacement was tracked using IMAGEJ and IMARIS software. Tracks were checked manually to ensure accurate particle tracking. Algorithms were written in MATLAB software to determine velocity, vorticity, strain, WSS, and vessel wall motion. Particle displacement error was estimated at most to be 0.25% without taking into account particle lag effects, which accounted for less than 1% due to the low Reynolds number flow. The measurement uncertainty of the calculated vorticity, strains, and WSS magnitudes is at most 20%. Lymphatic endothelial Prox1-GFP marker enabled lymphatic vessel edge detection and vessel motion tracking.

Particle Polyethylene Glycolylation. Briefly, the microspheres were incubated in 10 mM N-hydroxysuccinimide (Acros Organics, Geel, Belgium) and 20 mM N-ethyl-N'-(3-dimethylaminopropyl) carbodiimide hydrochloride (Sigma-Aldrich) for 1 h at room temperature to activate carboxylate groups on the microsphere surface. The solution was centrifuged, supernatant was removed, and particles were washed with 95% ethanol and air dried. Next, to amino-terminate polyethylene glycol (PEG) (Alfa Aesar, Haverhill, MA), PEG was incubated with the (3-aminopropyl) triethoxysilane (APTES) (Sigma-Aldrich) solution (2% by volume 3-aminopropyltriethoxysilane in 100% anhydrous ethanol) for 2 h at room temperature. The PEG solution was centrifuged, the supernatant was removed, and then rinsed with 95% ethanol. The supernatant was removed and the PEG solution gently dried with compressed air. Then, the chemically activated microspheres were incubated with the aminoterminated PEG for 30 min at room temperature to covalently bind PEG to the microsphere surface, in order to prevent microsphere aggregation and interaction with cells.

Region of Interest Defined. The flow field inside lymphatic vessels, distal from the inguinal lymph node, was quantified using fluorescent particle tracking (Figs. 1(*a*)–1(*c*)). The region of interest (ROI) for the normal mouse includes two lymphangions and a bileaflet valve, while the ROI for the affected mouse contains three lymphangions, two pairs of bileaflet valves as well as one congenital malformed unileaflet valve (Fig. 1(*c*)). Within each lymphangion, there are smaller segments where the lumen diameter was determined (Fig. 1(*c*)). The valves help facilitate net forward flow of lymph from right to left for both mice.

Stabilizing Images Due to Movement. To address the inherent tissue movement of the mice due to breathing, twitching, and sporadic muscle movements, an algorithm in MATLAB software was written to stabilize the images. The algorithm yielded a linear displacement for each image with relation to the first image in the series. The displacement data were used to stabilize the images and then used in a power spectral density (PSD) analysis to identify the most energetic tissue movements.

Velocity and Flow Rate Calculations. Individual particles were tracked for consecutive images acquired $\Delta t = 33.4$ ms apart. During the interimage acquisition time of Δt, particles shift Δx and Δy pixels in the horizontal and vertical directions, respectively. After calculating the particle displacement between consecutive images and dividing it by the time between each image acquisition, the two-dimensional velocity is calculated as follows:

$$\mathbf{V} = \frac{1}{M}\left(\frac{\Delta x}{\Delta t}\mathbf{i} + \frac{\Delta y}{\Delta t}\mathbf{j}\right) \tag{1}$$

where M is the magnification factor. The horizontal velocity component $\Delta x/(M \times \Delta t)$ parallel to the vessel wall was used to

Table 1 Primers for quantitative polymerase chain reaction mRNA analysis

Gene	Locus ID	Forward primer (5′–3′)	Reverse primer (5′–3′)	Fragment (bp)
ICAM-1	NM_000201.1	GCGTAGGGTAAGGTTCTTGC	GCTATTCAAACTGCCCTGATG	128
ICAM-2	NM_000873.5	ACTCAATGGTGAAGGACTTGC	TCCAATGCCACTTCACCTG	135
JAM-A	NM_016946.1	TGACTTCAGGTTCAGAAGAGTG	GCAAGTCGAGAGGAAACTGT	101
LYVE-1	NM_006691.1	CCATAATTCTGCATGACACCTG	ATCTGGACCACGAGGCT	79
CCL2	NM_002982.1	GCCTCTGCACTGAGATCTTC	AGCAGCCACCTTCATTCC	104
CXCL2	NM_002089.4	CATCGAAAAGATGCTGAAAAATG	TTCAGGAACAGCCACCAATA	77
IL-8	NM_000584.1	CTTCACACAGAGCTGCAGAA	GAGACAGCAGAGCACACAAG	143
GAPDH	NM_002046.1	TGTAGTTGAGGTCAATGAAGGG	ACATCGCTCAGACACCATG	143

Table 2 Primary and secondary antibodies for Western Blot analysis

Antibody	Host species	Vendor	Catalog #	Working dilution
ICAM-1	Rat	Santa Cruz Biotechnology, Dallas, TX	sc-52553	1:500
ICAM-2	Mouse	Santa Cruz Biotechnology, Dallas, TX	sc-9987	1:500
JAM-A	Rabbit	Thermo Fisher Scientific, Waltham, MA	36-1700	1:250
LYVE-1	Rat	R&D Biosystems, Minneapolis, MN	MAB2125	1:500
β-Tubulin	Mouse	Santa Cruz Biotechnology, Dallas, TX	166729	1:1000
Goat IgG HRP	Rabbit	Invitrogen, Carlsbad, CA	81-1620	1:1000
Mouse IgG HRP	Goat	Thermo Fisher Scientific, Waltham, MA	31430	1:1000
Rabbit IgG HRP	Goat	Thermo Fisher Scientific, Waltham, MA	31460	1:1000
Rat IgG HRP	Goat	Thermo Fisher Scientific, Waltham, MA	31470	1:1000

determine the radial velocity distribution along the height of the vessel within a planar segment (Fig. 1(*c*)). Velocity vectors determined from the particle shift within a planar segment were used to calculate a segment flowrate, Q^*, defined as follows:

$$Q^* = \text{Area} \times \text{Average velocity for segment} = \frac{\pi D^2}{4} \times \frac{1}{D} \int_{-D/2}^{D/2} u(y)dy \quad (2)$$

where the lymphatic vessel cross-sectional geometry is approximated as a circle, D is the diameter of the vessel and height of the longitudinal plane in the main flow direction, u is the velocity along the length of the vessel, and y is the integration variable in the vertical direction within the longitudinal plane along the main axis of the vessel. The average velocity, $\bar{u}$, for the segment was determined within a plane from the Simpson's 1/3 rule for each segment in Fig. 1(*c*).

Cell Culture. Human dermal lymphatic endothelial cells (PromoCell; Heidelberg, Germany) in passages 2–10 were cultured in EGM-2 MV cell medium (Lonza; Basel, Switzerland). Cells were grown to confluence on $75 \times 38\,\text{mm}^2$ borosilicate glass slides (Fisher Scientific; Waltham, MA) coated with gelatin (Eastman; Rochester, NY) to promote adhesion. Experiments were conducted at least 2 days after cells reaching 100% confluence.

Quantitative Reverse Transcription Polymerase Chain Reaction. Reverse transcription and quantitative real-time polymerase chain reaction was conducted using the CFX Connect Real-Time Polymerase Chain Reaction (PCR) Detection System (Bio-Rad Laboratories; CA). Immediately upon termination of the in vitro flow experiments, total RNA was extracted from cells in static culture and from cells exposed to flow using the RNEasy Plus Mini Kit isolation reagents (QIAGEN; Hilden, Germany). Extracted RNA was reverse transcribed to complementary DNA using iScript gDNA Clear cDNA Synthesis Kit (Bio-Rad Laboratories; CA) and amplified with the iQ SYBR Green Supermix (Bio-Rad Laboratories; CA) to identify relative expression of IL-8, CCL2, CXCL2, ICAM-1, ICAM-2, JAM-A, and LYVE-1 mRNA. Results from the in vitro cultured lymphatic endothelial cells were normalized to those of human GAPDH. The sequences of the primers used are shown in Table 1.

Western Blotting. After the 48 h experiment of either static or lymphatic-like waveform, protein was extracted by lysing the cells for 1 h in 10% RIPA (Cell Signaling Technology; Danvers, MA) containing MG132 protease inhibitor (Tocris Bioscience; Bristol, UK), and Halt protease inhibitor (Life Technologies; Carlsbad, CA), and Halt phosphatase inhibitor (Life Technologies; Carlsbad, CA) at 4 °C, centrifuging at $13{,}000 \times g$, and discarding the cell pellet. The Western blot was conducted by separating 20 μg of protein by 10% SDS-PAGE gel (Bio-Rad Laboratories; CA) and transferring to a PVDF membrane (Invitrogen; Carlsbad, CA). After transferring, the PVDF membrane was incubated in a blocking buffer of PBS with 0.1% Tween-20 and 5% milk for 1 h at room temperature and probed overnight at 4 °C with the primary and secondary antibodies listed in Table 2. The membrane was rinsed and incubated with HRP-conjugated antibody for 1 h at room temperature. Femto-Chemiluminescent substrate (Thermo Fisher Scientific; Waltham, MA) was used. Digital images were acquired with the ChemiDoc Touch imager (Bio-Rad Laboratories; CA). Densitometric band analysis was performed with Image

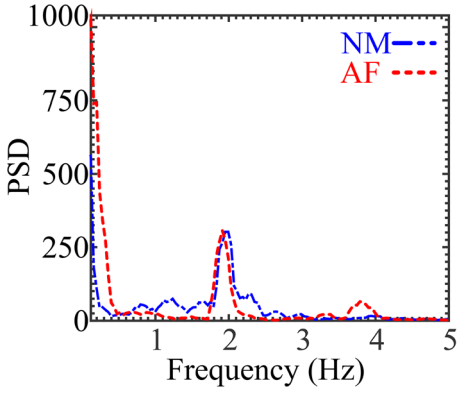

Fig. 2 PSD analysis from mice shows the most energetic tissue movements around 2 and 1.9 Hz for the normal and affected mice, respectively

Multi-Gauge Software (Fujifilm; Tokyo, Japan) and normalized to the levels of β-tubulin or β-actin.

Results

Image Movements Elucidate Breathing Rates. The PSD analysis yielded two curves with multiple peaks due to inherent tissue movement. The largest peaks were present at 0 Hz, which corresponds to the DC-offset and is not physiological, but inherent to the analysis. The second most energetic peaks were present at approximately 2 and 1.9 Hz for the normal and affected mice, respectively. These peaks correspond to tissue movement interpreted as the breathing rate, which ranged from 120 to 114 times per minute for the normal and affected mice, respectively (Fig. 2).

Intra- and Interanimal Heterogeneity Dictates Vessel Contractility. The smooth muscle cell media layer in collecting lymphatic vessels aids in pumping lymph [23–25]. However, the vessel regions that coincide with valves are void of smooth muscle cells and experience less contraction. To determine the degree of contractility throughout the lymphangion, three regions were analyzed (Figs. 3(*a*) and 3(*b*)). For the normal mouse, two segments coincided with the center of each lymphangion, where maximum contractility would be expected given its distance from the valve, and the third segment was within one vessel diameter (D) from the bileaflet valve (Fig. 3(*a*)). For the affected mouse, one segment coincided with the center of the lymphangion, while the other two were next to the lymphatic valves, including the unileaflet valve (Fig. 3(*b*)). The EC Prox1-GFP expression enabled

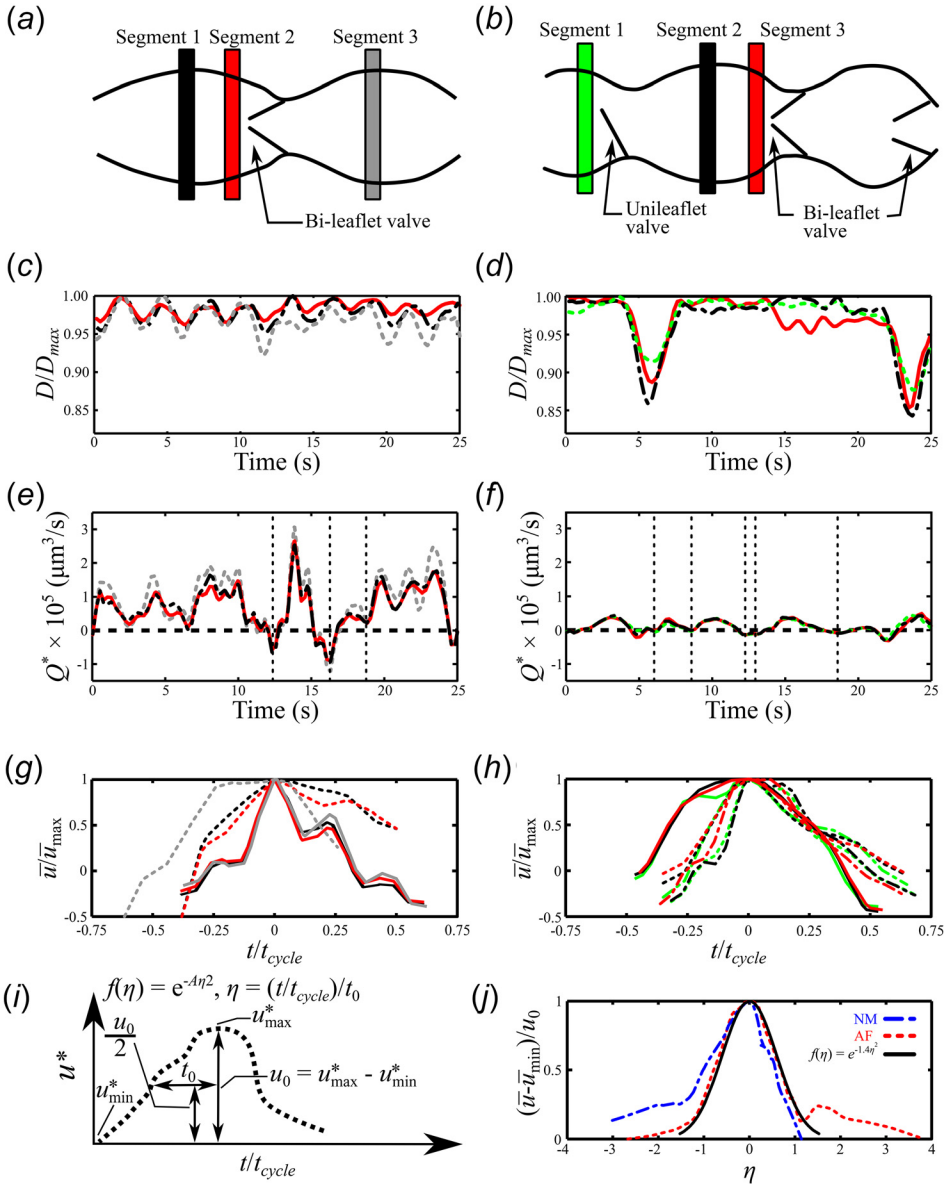

Fig. 3 Schematic of the lymphangions highlighting the different isolated segments for the (*a*) normal and (*b*) affected mice. The local diameter of each segment is normalized by the maximum lymphatic diameter in the ROI and plotted as D/D_{max} for the (*c*) normal and (*d*) affected mice. The segment flowrate, Q^*, for the (*e*) normal and (*f*) affected mice. Vertical gridlines shown in (*e*) and (*f*) denote the start and end points for the individual cycles in (*g*) and (*h*). The mean velocity, $\bar{u}$, value is nondimensionalized by the max mean velocity, $\bar{u}_{max}$, and plotted for both the (*g*) normal and (*h*) affected mice. The different colors and line styles correspond to different segments and lymph velocity cycles, respectively. (*i*) Schematic detailing the relationships used to determine (*j*) a representative general velocity function for the lymph velocity cycle where u_0 was calculated with respect to the right side of the curves.

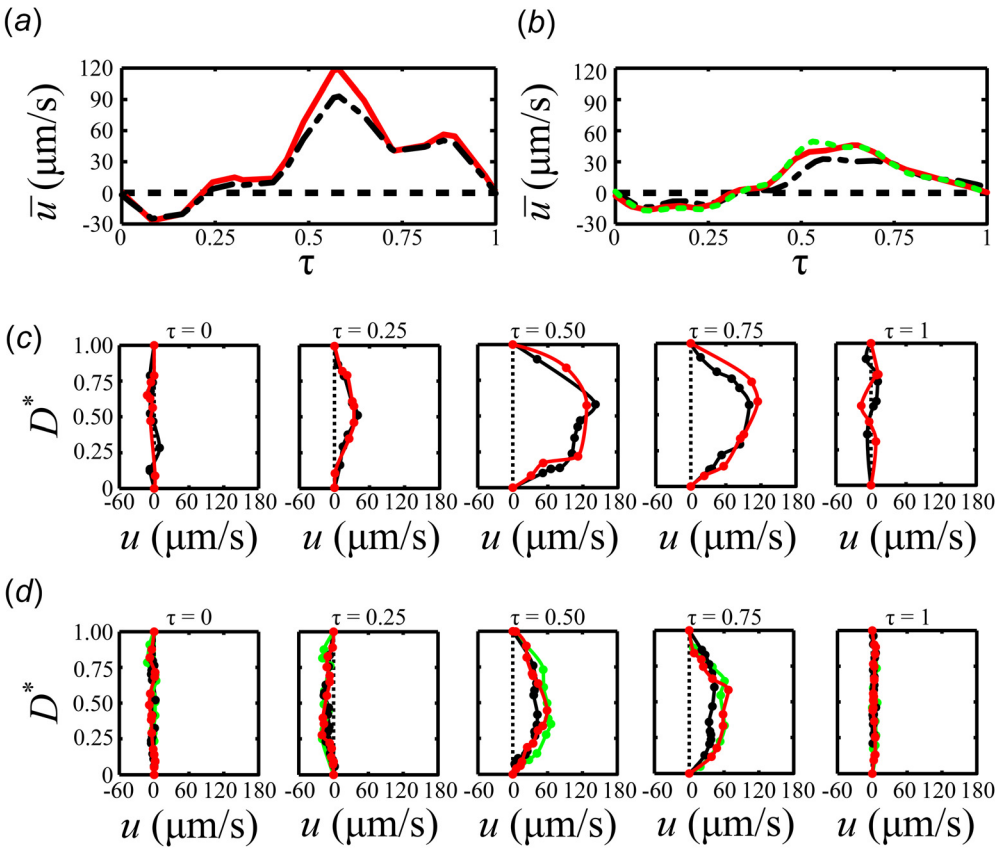

Fig. 4 The mean velocity, $\bar{u}$, within the midlymphangion (ML) (- —— -), downstream from the bileaflet valve (—), and immediately downstream from the unileaflet valve (- - -) segments for the (*a*) normal and (*b*) affected mice. The radial velocity profile at the ML (—), downstream from the bileaflet valve (—), and immediately downstream from the unileaflet valve (—) segments are plotted for the nondimensionalized intervals $\tau = 0$, 0.25, 0.5, 0.75, and 1 for the (*c*) normal and (*d*) affected mice.

tracking of the vessel wall motion in order to quantify the instantaneous local lumen diameter and vessel contractility. Figure 3(*c*) shows the lymphatic vessel normalized diameter as a function of time for all analyzed segments of the normal mouse (Fig. 3(*a*)). The diameter is normalized by the maximum vessel diameter (D_{max}) within the ROI. When the vessel is fully relaxed at a segment, D/D_{max} equals 1 and D/D_{max} decreases as the vessel contracts. The segments in the center of the lymphangion displayed greater contractility, ranging between 4.7% for segment 1 and 7.8% for segment 3, whereas the segment closest to the bileaflet valve (segment 2) of the normal mouse contracted at most 3.75%. Similarly, the center segment of the lymphangion of the affected mouse (segment 2) contracted the greatest with a maximum contractility of 15.7% (Fig. 3(*d*)). When comparing the different segments of the affected mouse, the segment next to the unileaflet valve contracted the least with a maximum contraction of 12.3%. The maximum contraction of the normal mouse vessel was 7.8%, compared to 15.7% in the affected mouse. Contraction frequency for the time observed was 0.34 and 0.06 Hz for the normal and affected mice, respectively. While the spatial and temporal diameter changes are heterogeneous, the segments in the center of the lymphangions tend to yield the largest contractions.

Net Antegrade and Retrograde Flow Present in Collecting Lymphatic Vessels. The segment flow rate for the normal mouse ranged between 3.1×10^5 and -1.2×10^5 $\mu m^3/s$, while the affected mouse experienced Q^* between 4.3×10^4 and -3.1×10^4 $\mu m^3/s$ (Figs. 3(*e*)–3(*f*)). For all analyzed segments, the segment flowrate Q^* for both mice is characterized by periods of net antegrade and retrograde flow, even in the presence of functional bileaflet valves. While larger amplitude and frequency fluctuations in Q^* were observed for the normal mouse in the period analyzed, these values are highly heterogeneous within the mouse and when compared to other normal mice (data not shown).

The absence of a central pumping organ results in highly variable flow rates. However, the fundamental elements that cause movement of lymph are similar. Hence, we propose a representative general velocity relationship that describes a velocity period in the collecting vessel distal of the inguinal lymph node. First, we isolated distinct cycles from the segment flowrate determined in Figs. 3(*e*) and 3(*f*). Cycles are based on local minima and maxima given that lymph flow cycles vary from one cycle to the next. Since each cycle varies in time, the time is normalized to a value of 1 by dividing the time variable t by the total time of the cycle, t_{cycle}. The average velocity is nondimensionalized by the maximum average velocity, $u^* = \bar{u}/\bar{u}_{max}$, (Figs. 3(*g*) and 3(*h*)). Following the relationship detailed in Fig. 3(*i*), we find the value of t/t_{cycle} at $u_0/2$, where $u_0 = (u^*_{max} - u^*_{min})$. We call this value t_0. Two cycles were selected from Fig. 3(*e*). The first cycle started and ended at 12.4 and 16.3 s, respectively, while the starting point of the second cycle coincided with the end of the first cycle and ended at 18.8 s. From Fig. 3(*f*), three cycles were selected. The start points for the three cycles are 6, 8.6, and 13 s, while the end points are 8.6, 12.3, and 18.7 s, respectively. Each of these asymmetric velocity curves have two possible t_0 values and the value from the right side of the curve was chosen. Using these values, we can propose a function $f(\eta)$ that can describe the mean velocity periods in these lymphatic vessels. Next, we calculate $f(\eta) = e^{-A\eta^2}$ where $\eta = (t/t_{cycle})/t_0$ and $A = 1.40\,s^2$, and plot it along with the average of the normalized velocity period for both the normal and affected mice (Fig. 3(*j*)). The resulting normalized

velocity periods for both animals demonstrate a representative general velocity function and it is described by $f(\eta) = e^{-1.40\eta 2}$.

Lymphatic Radial Velocity Profile is Not Parabolic. One velocity period for each mouse was isolated from Figs. 3(*e*) and 3(*f*) as shown in Figs. 4(*a*) and 4(*b*). The time variable, τ, for the velocity periods is normalized to range between τ equals 0 and 1, since inter- and intra-animal variations of velocity periods can vary significantly. The radial velocity distribution is plotted for five different instances in the normalized period for the normal and affected mice (Figs. 4(*c*) and 4(*d*)). Each radial velocity distribution was composed of 7–17 data points and a spline function was used to fit a curve to the data points. Given that the lymphatic vessel is contracting and dilating throughout the period, the lumen diameter is normalized as $D^* = D/D_{\text{Local}}$ where $D^* = 0$ and $D^* = 1$ are the bottommost and uppermost parts of the lumen wall, respectively. Figures 4(*a*) and 4(*c*) show that at $\tau = 0$, the net velocity is approximately 0 for both segments 1 and 2 of the normal mouse. The net lymph flow reverses and Q^* reaches a minimum at $\tau = 0.081$ before moving once again in the antegrade direction around $\tau = 0.25$ (Figs. 4(*a*) and 4(*c*)). As the period approaches $\tau = 0.5$, the lymph flow continues to accelerate until $\tau = 0.58$ where Q^* reaches a maximum. A close look at the radial velocity distribution reveals that the flow across the entire vessel in the middle segment is moving in the antegrade direction, while not completely parabolic due to the three-dimensionality introduced by the valve. As the cycle approaches $\tau = 0.75$, the lymph flow velocity in the segment near the valve reaches a local minimum, while the flow is fully antegrade across the vessel. As the period approaches $\tau = 1$, lymph flow decelerates toward 0 mm/s and the radial velocity distributions for both segments become flatter with local pockets of both antegrade and retrograde flow.

Similar to the normal mouse, the lymph flow period in the affected mouse is characterized by pulsatility (Fig. 4(*b*)). The radial velocity distribution at $\tau = 0$ for the segments in the middle of the lymphangion and near the affected and normal valves show a combination of small segments of antegrade and retrograde flow (Fig. 4(*d*)). Q^* reaches its minimum at $\tau = 0.23$ before it starts to accelerate in the antegrade direction. As the cycle starts to accelerate around $\tau = 0.25$ and approaches $\tau = 0.5$, the radial velocity profiles show fully antegrade, but asymmetric flow. The flow continues to accelerate until Q^* reaches its maximum at $\tau = 0.53$ and starts to decelerate thereafter. The asymmetry in the radial velocity distribution is still evident at $\tau = 0.75$ as the flow decelerates toward $\tau = 1$, where the flow velocity reaches approximately 0 μm/s for all segments of the affected mouse.

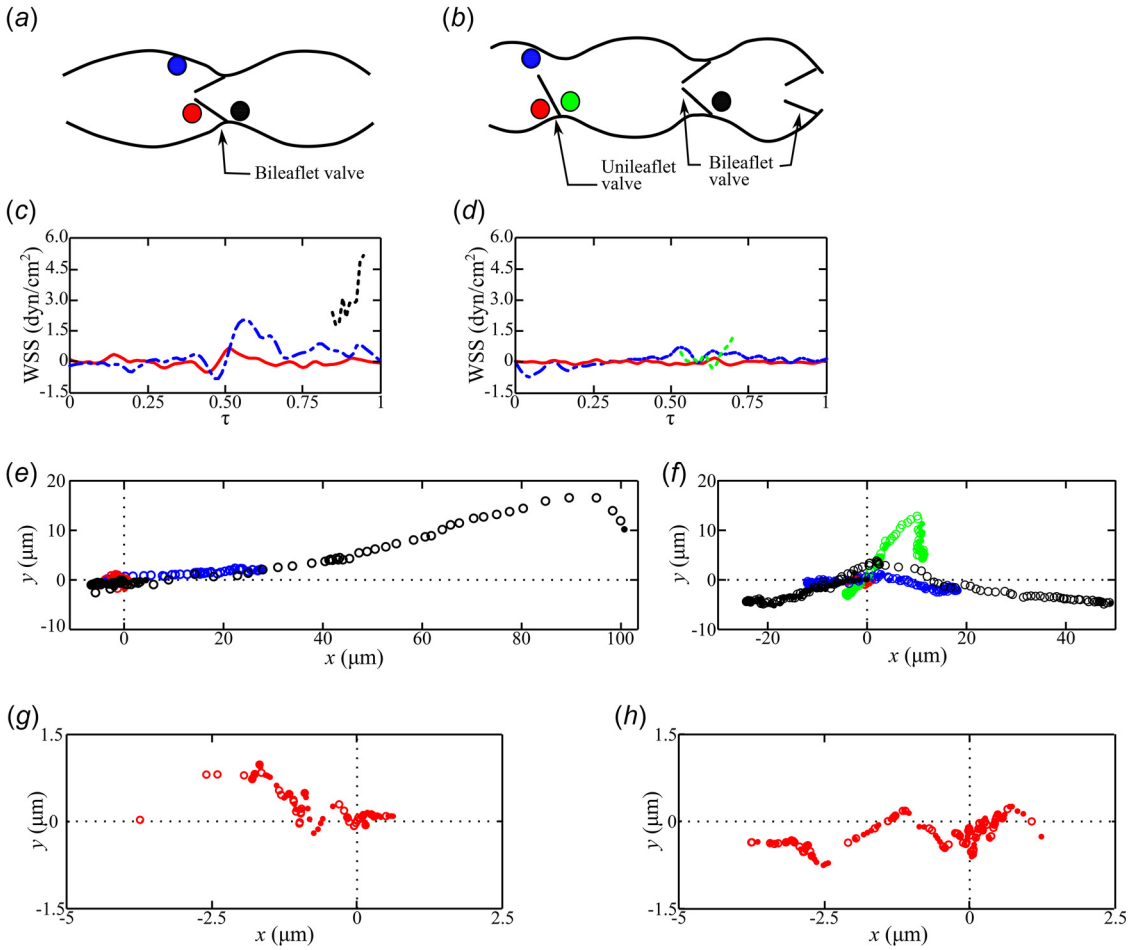

Fig. 5 A schematic demonstrates the initial location of the individual particles that were tracked inside the lymphatic vessels of the (*a*) normal and (*b*) affected mice. WSS is plotted, only when particles are traversing adjacent to a vessel surface, for the particles upstream of the bileaflet (- - -) and unileaflet (- - -) valves, along the lymphangion surface (- — -), and inside the recirculation zone (—) for the (*c*) normal and (*d*) affected mice. The particle coordinates are plotted for each time-step as the particles move in the antegrade (○) and retrograde (●) lymph flow directions for the particles upstream of the bileaflet (○,●) and unileaflet (○,●) valves, along the lymphangion surface (○,●), and inside the recirculation zone (○,●) for the (*e*) normal and (*f*) affected mice. Given the short displacement of the particles in the recirculation zone (○,●), the coordinates are replotted in with different axes limits for the (*g*) normal and (*h*) affected mice.

Decreased Wall Shear Stress in Vessel Containing Unileaflet Valve. The trajectories of individual particles were tracked in the normal (Fig. 5(*a*)) and affected (Fig. 5(*b*)) mice during the nondimensionalized periods, τ, shown in Figs. 4(*a*) and 4(*b*). Three particles were tracked close to the bileaflet and unileaflet valves in the normal and affected mice, respectively. A fourth particle was tracked proximal to a bileaflet valve in the affected mouse (Fig. 5(*b*)). The WSS magnitude for the various particle paths is shown for the normal (Fig. 5(*c*)) and affected (Fig. 5(*d*)) mice. These particles were selected because they traveled tangentially along a surface, enabling an estimation of the WSS. WSS is only plotted when a particle is next to the wall. Given that the particles are PEGylated, their interaction with the wall is minimal and movement is primarily due to the lymph flow. Heterogeneity can be observed when comparing lymph flow in different locations in the vessel and when comparing different animals. The normal mouse experienced a minimum WSS magnitude of 0 dyn/cm^2 and a maximum WSS of 5.1 dyn/cm^2 along the surface of the bileaflet valve, compared to 0 and 1.4 dyn/cm^2 on the surface of the unileaflet valve of the affected mouse. WSS was lowest for both mice in the recirculation zones next to the valves with WSS ranging between −0.49 and 0.67 dyn/cm^2 for the normal mouse, and −0.14 and 0.20 dyn/cm^2 for the affected mouse. The particle along the upper wall of the vessels of both mice rests further distally along the wall and is affected much less by the valve, resulting in greater WSS magnitudes of up to 2 and 0.79 dyn/cm^2 for the normal and affected mice, respectively. The differences in WSS of the unileaflet valve become evident when comparing the WSS magnitudes along the surface of the valve, based on a representative sample particle track. The WSS values experienced along the surface of the normal bileaflet valve were much greater than those experienced on other walls of the lymphangion (Fig. 5(*c*)). In contrast, the WSS amplitude on the surface of the unileaflet valve was comparable to other surfaces on the lymphangion (Fig. 5(*d*)).

Endothelial cells in the lymphangion were exposed to different lymph flow waveforms that differed in WSS magnitudes and oscillatory shear index (OSI). The OSI value quantifies the extent to which the ECs experience retrograde flow throughout the velocity cycle, and it is determined by the following equation:

$$\mathrm{OSI} = \frac{1}{2}\left(1 - \frac{\left|\int_0^T \tau_w \mathrm{d}t\right|}{\int_o^T |\tau_w| \mathrm{d}t}\right) \tag{3}$$

where T is the upper limit of integration corresponding to the length of time of the lymph flow velocity cycle and τ_w is the wall shear stress [26]. The OSI equals 0 for a fully antegrade waveform, and 0.5 for an equally bidirectional flow. The OSI for the particles traveling along the wall downstream of the valves equaled 0.15 and 0.32 for the normal and affected mice, respectively. Inside the recirculation zones, the OSI were 0.46 for both the normal and affected mice.

Lymph Particle Residence Time is Strongly Affected by Valve Presence. Trajectories for the particles selected in Figs. 5(*a*) and 5(*b*) are shown in displacement plots in the x (axial) and y (vertical) directions for the normal (Figs. 5(*e*) and 5(*g*)) and affected (Figs. 5(*f*) and 5(*h*)) mice. In the normal mouse, lymph flows through the bileaflet valve in both the antegrade and retrograde directions, and has higher momentum based on its larger displacement relative to the particle traveling along the wall and in the recirculation zone (Fig. 5(*e*)). During the period τ, the particle through the bileaflet valve was displaced 145 μm, while the

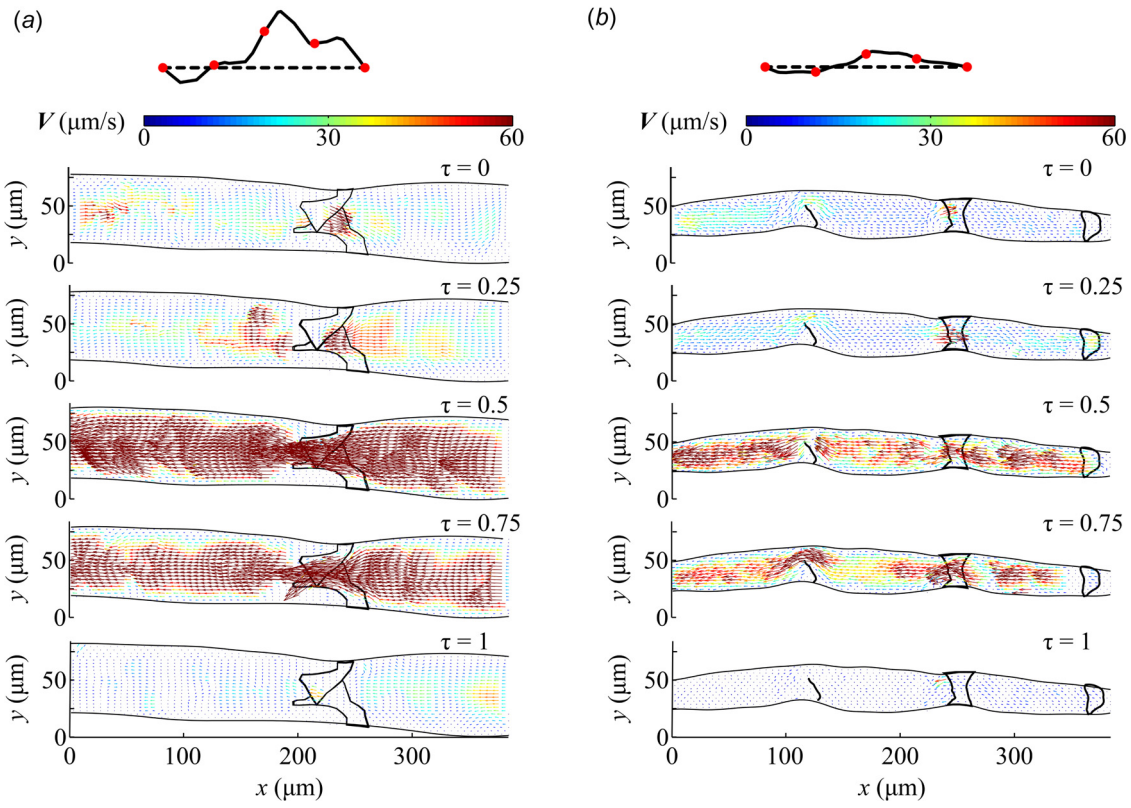

Fig. 6 The lymph velocity vector field inside lymphatic vessels, distal from the inguinal lymph node, for the (*a*) normal and (*b*) affected mice at five separate points in a mean velocity cycle, $\tau = 0$, 0.25, 0.5, 0.75, and 1.0. The wall and outline of the valves are shown. The flow waveform is shown with red circles denoting the five different time points.

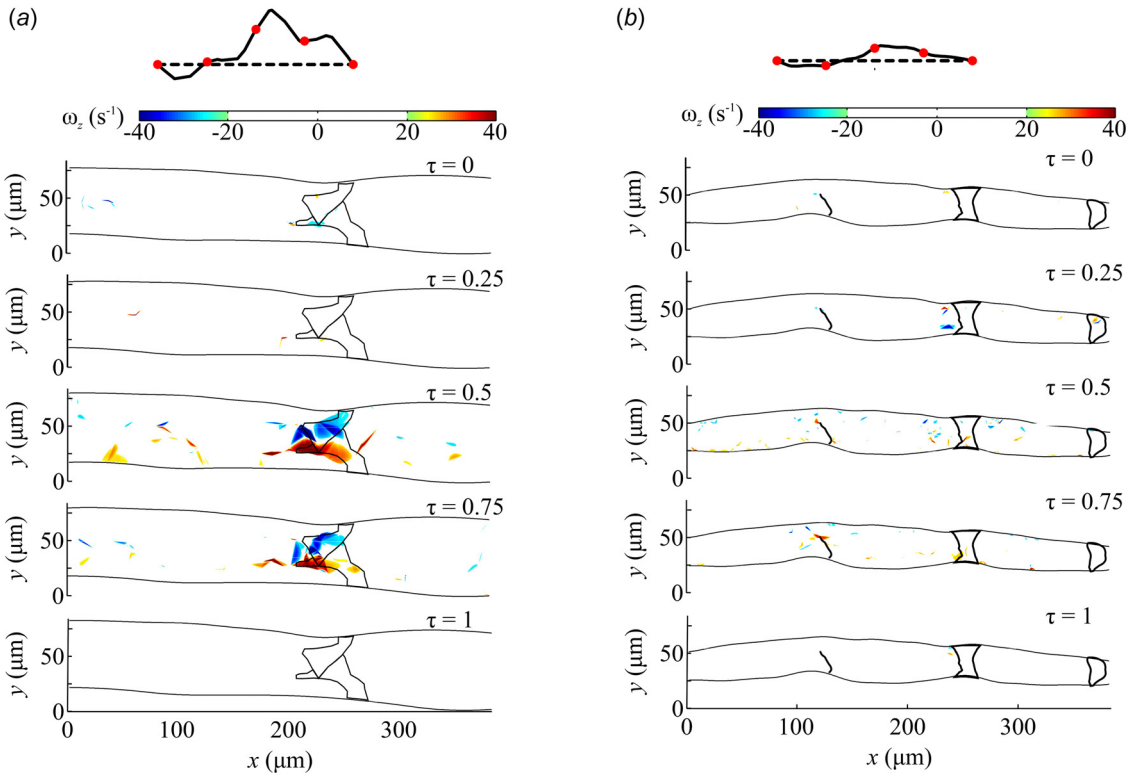

Fig. 7 The lymph vorticity field inside lymphatic vessels, distal from the inguinal lymph node, for the (*a*) normal and (*b*) affected mice at five separate points in a mean velocity cycle, $\tau = 0$, 0.25, 0.5, 0.75, and 1.0. The wall and outline of the valves are shown. The flow waveform is shown with red circles denoting the five different time points.

particles distal from the valve and inside the recirculation zone only traveled 27.9 and 2 μm, respectively. In contrast, the particle through the unileaflet valve was only displaced 12.1 μm, while those along the upper wall and recirculation zone traveled 18.6 and 3 μm (Fig. 5(*f*)). To demonstrate that the differences in particle trajectory between animals was not completely due to anatomical differences, a particle was tracked as it was displaced through a bileaflet valve of the affected mouse showing that the displacement was 60% greater than that through the unileaflet valve. This difference in displacement may result from differences in wall proximity. The particle flowing through the bileaflet valve of the affected mouse has a higher net displacement in the axial direction than the particle traveling through the unileaflet valve. The particle traveling through the unileaflet valve travels less in the axial direction, but more in the vertical direction. This demonstrates that the malformed valve redirects lymph flow toward the vessel wall. The displacement of particles inside the recirculation zones immediately distal from the valves is shown in the normal (Fig. 5(*g*)) and affected (Fig. 5(*h*)) mice. The net displacement in these recirculation zones is at most 3 μm, indicating increased particle residence time and limited transport compared to particles traveling along the vessel wall or through the valves.

Bileaflet Valves Concentrate High Velocity Flow in Center, While Unileaflet Valve Skews High Velocity Flow Toward Vessel Wall. Figure 6(*a*) shows the velocity vector field for five instances during a velocity cycle of the normal mouse. The measured particle displacements were interpolated, yielding uniform velocity vector fields inside the lymphatic vessels. During $\tau = 0$, even in the presence of an intact bileaflet valve, retrograde flow dominates the flow field. In contrast, at $\tau = 0.25$ flow directionality has completely shifted to the antegrade direction. As the flow accelerates, faster flow extends to the near-wall regions except in the recirculation zones created by the bileaflet valve. As flow decelerates at $\tau = 0.75$, faster flow moves away from the near-wall region to the center of the vessel until $\tau = 1$, where the fastest lymph flow is observed as it accelerates through the bileaflet valve. Although inter- and intra-animal lymphatic flow heterogeneity exists, the predominant flow characteristics observed, including flow reversal, slow moving recirculation zones and accelerated flow are representative of efferent lymph flow distal from the inguinal lymph node (data not shown).

Figure 6(*b*) shows the flow field for an affected mouse with two pairs of bileaflet valves and a unileaflet valve. At $\tau = 0$, where flow is quiescent, local high velocity pockets are present at valves with flow moving in the retrograde direction. At $\tau = 0.25$, the flow velocity is near its minimum value before it accelerates toward $\tau = 0.5$. Flow directionality at both bileaflet valves (center and rightmost valves) is primarily symmetric. In contrast, the flow field in the vicinity of the unileaflet valve is skewed with high velocity lymph flow diverted toward the upper vessel wall and a large recirculation downstream of the unileaflet valve. This trend continues at $\tau = 0.75$ before decelerating to quiescent flow at $\tau = 1$.

Majority of Vorticity is Generated at Valves. From the velocity vector field, we determined the vorticity field, which is defined mathematically as the curl of the velocity

$$\omega_z = \frac{dv}{dx} - \frac{du}{dy} \tag{4}$$

where u and v are the axial and vertical components of velocity, respectively. In the context of lymphatic vessels, vorticity represents the local lymph rotation. In the normal mouse, before $\tau = 0.50$, the levels of vorticity are close to zero. As lymph flow accelerates from $\tau = 0.50$ to 0.75, vorticity increases significantly at the valve to a maximum value of -79.2 and $119.4\,s^{-1}$, where

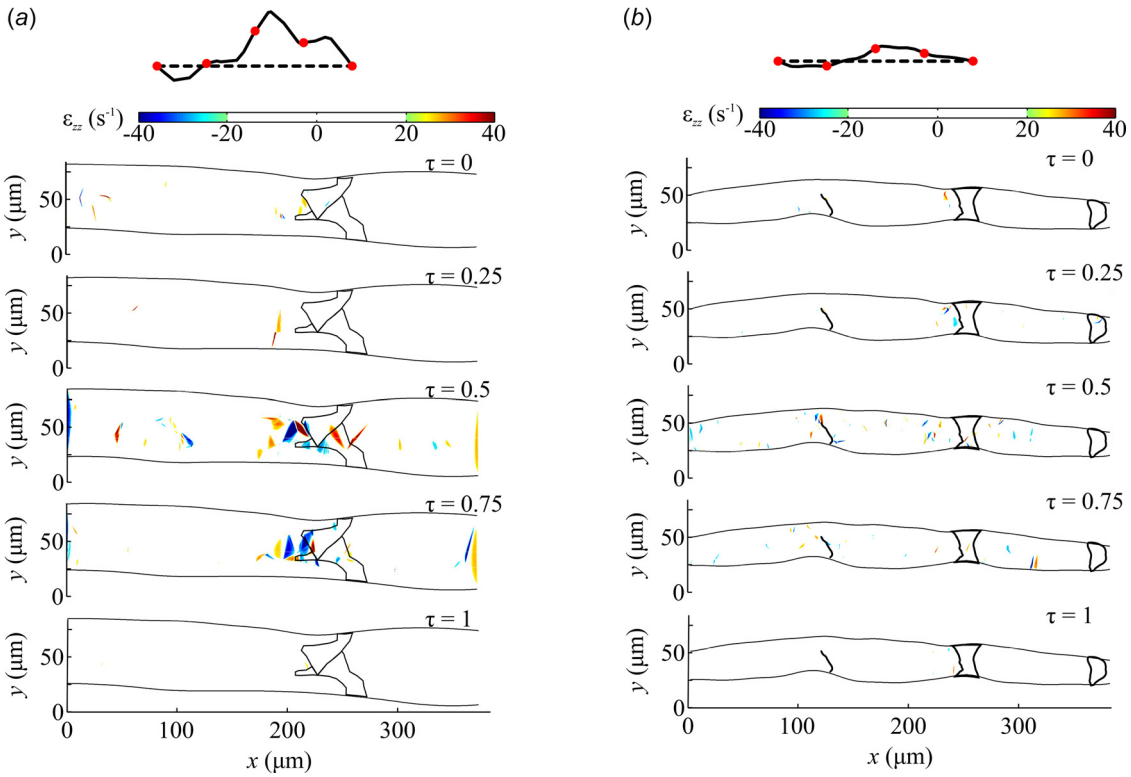

Fig. 8 The lymph normal strain field inside lymphatic vessels, distal from the inguinal lymph node, for the (*a*) normal and (*b*) affected mice at five separate points in a mean velocity cycle, $\tau = 0$, 0.25, 0.5, 0.75, and 1.0. The wall and outline of the valves are shown. The flow waveform is shown with red circles denoting the five different time points.

positive and negative values denote clockwise and counterclockwise rotational orientation, respectively (Fig. 7(*a*)). As the flow decelerates toward $\tau = 1$, vorticity decreases to zero.

Similar to the normal mouse, vorticity in the affected mouse was near zero at time $\tau = 0$, 0.25, and 1 with local pockets of high vorticity near the valve. At $\tau = 0.50$, vorticity increases in the vessel as velocity increases, especially toward the center of the vessel, with a max vorticity of 74.7 s^{-1} (Fig. 7(*b*)). At $\tau = 0.50$ and 0.75, greater vorticity values are present closer to the walls near the left unileaflet (left) and the center bileaflet valves, as a result of the three-dimensional flow promoted by the valves. This near-wall vorticity could not be appreciated in the normal mouse given that these leaflets are offset about 90 deg and the imaging planes do not coincide. In the affected mouse, the highest vorticity values are observed along the surface of the unileaflet valve (left), especially along the wall, due to the momentum of the flow directed toward the vessel wall at $\tau = 0.50$ and 0.75.

Valves Induce Increases in Normal and Shear Strain Rates. The normal and shear strain rates were determined, respectively, from the velocity vector field as follows:

$$\varepsilon_{zz} = \frac{du}{dx} + \frac{dv}{dy} \tag{5}$$

$$\varepsilon_{xy} = \frac{du}{dy} + \frac{dv}{dx} \tag{6}$$

The normal strain and shear strain rate values for the normal and affected mice for $\tau = 0$, 0.25, and 1 were predominantly zero with local pockets of high strain near the valve (Figs. 8 and 9). As the lymph velocity increased inside the lymphatic vessel of the normal mouse at $\tau = 0.50$ and 0.75, the normal and shear strains increased along the core of the flow with peak values at the valve reaching maxima of 81 and –120 s^{-1} for ε_{zz} and ε_{xy}, respectively (Figs. 8(*a*) and 9(*a*)). Very similar results are observed for the affected mouse, except for increased normal and shear strain values near the wall of the unileaflet valve due to the skewing of the lymph toward the wall (Figs. 8(*b*) and 9(*b*)). At the unileaflet valve, the maximum normal strain decreased from −79.7 s^{-1} to −62.8 s^{-1} from $\tau = 0.50$ and 0.75, respectively. Similarly, the shear strain decreased from –73.9 s^{-1} to −52.6 s^{-1} from $\tau = 0.50$ and 0.75, respectively.

Lymph Flow Pathlines Denote Four Distinct Flow Regions. Figures 10(*a*) and 10(*b*) show particle pathlines determined from the trajectory of fluorescent particles in the lymphangion of the normal and affected mice during 22.5 s. The pathlines delineate a heterogeneous flow field characterized by four different regions: midlymphangion (ML), in-side of lymphatic valves, recirculation zones, and valvular sinus (VS, Fig. 11). The flow in the midlymphangion region is primarily denoted by parallel pathlines that start to converge as the flow approaches the lymphatic valves. The flow accelerates to its maximum velocity as it traverses through the lymphatic valves (in-side) causing a flow separation that yields recirculation zones on the opposite side of the valve leaflets. In the recirculation zones, the flow is primarily moving at a very low velocity in the opposite direction of the bulk lymph flow, while the bulk flow is decelerating as it approaches the midlymphangion region of the neighboring lymphangion. Flow tracking measurements from multiple mice (data not shown) showed that flow is practically static in the valvular sinus where the leaflets join the vessel wall.

Quasi-Static Lymph Flow Conditions in the Valvular Sinus Milieu Promote a Pro-Inflammatory Phenotype. Lymph flow measurements derived from mice were used to construct in vitro fluid flow waveforms representative of the ML and VS regions

(Fig. 10(*c*)). To determine the effects of lymph flow heterogeneity on LEC phenotype, LECs were exposed in vitro to either of these two flow conditions for 48 h using our previously described parallel plate flow chamber system [27].

Because of the importance of the lymphatic system in regulating an inflammatory response, the gene and protein expressions of various chemokines (IL-8, CCL2, and CXCL2) and cellular adhesion molecules (ICAM-1, ICAM-2, JAM-A, and LYVE-1) known to mediate endothelial transmigration of leukocytes in the blood circulatory system were probed (Figs. 10(*d*)–10(*f*)). Of the various genes probed, only LYVE-1 expression has been shown in LECs to be sensitive to lymphatic flow in vitro [16]. ICAM-1, IL-8, CCL2, and CXCL2 expression have been shown to be shear sensitive in circulatory ECs, but it is unknown if LECs will respond similarly, especially in the context of lymphatic relevant flow conditions [28–32]. To our knowledge, expression of ICAM-2 and JAM-A have not been previously demonstrated to be regulated by fluid shear stress in ECs originating from lymphatic or blood vessels.

The LECs subjected to the static VS condition for 48 h uniformly expressed higher mRNA expression of cellular adhesion molecules ICAM-1, ICAM-2, JAM-A, and LYVE-1 by 3.9-, 1.8-, 1.4-, and 13.5-fold, respectively, in comparison to the pulsatile ML waveform. Similarly, the LEC mRNA expression of transmigration relevant chemokines IL-8, CCL2, and CXCL2 was upregulated 8.2-, 5.8-, and 4.3-fold, respectively, when exposed to the static VS condition. LEC protein expression was also uniformly upregulated by 1.74-, 1.46-, 1.37-, and 1.48-fold for cellular adhesion molecules ICAM-1, ICAM-2, JAM-A, and LYVE-1, respectively, under static VS conditions. Protein measurements for secreted transmigration relevant chemokines IL-8, CCL2, and CXCL2 was not possible given the low protein concentration in our high cell medium volume system.

Discussion

To the best of our knowledge, this is the first study to characterize in vivo the local flow field in the inguinal lymph node efferent lymphatic vessels of adult mice and to connect different flow environments present in the lymphangion to a LEC proinflammatory phenotype. This study demonstrates the heterogeneous nature of lymphatic flow and shows that valve morphology affects the directionality of lymph flow. It is the first demonstration that the unique anatomy of lymphatic valves promotes higher flow velocity in the center of the vessels accompanied by near zero velocity extending beyond the near-wall region, significantly veering from the Poiseuille flow. However, valve malformation changes the flow profile by skewing lymph flow toward the vessel wall endothelium with potential clinical consequences. The lymphatic valve to lymph flow relationship also greatly influences local shear forces and transport of molecules with unknown consequences. Exposing LECs in vitro to the near stagnant lymph flow conditions present in the valve sinus elicited a proinflammatory phenotype in comparison to midlymphangion pulsatile flow conditions.

Lymph propulsion is regulated by local and distant elements, such as lymph vessel contractions, skeletal muscle movement, and changes in interstitial pressure. As the lymph intraluminal pressure increases, the circumferential stress that smooth muscle cells experience increases, activating contractility pathways. These contractility pathways, regulated by ion channels, are critical for the propulsion of lymph [23–25]. Although maximum lymph propulsion may be expected when neighboring lymphangions contract sequentially, our studies demonstrate that maximum propulsion is less predictable, emphasizing the interdependence of lymph propulsion with local and distant elements. These local and distant elements are responsible for rendering retrograde flow, even in the presence of normal bileaflet valves. Given that the

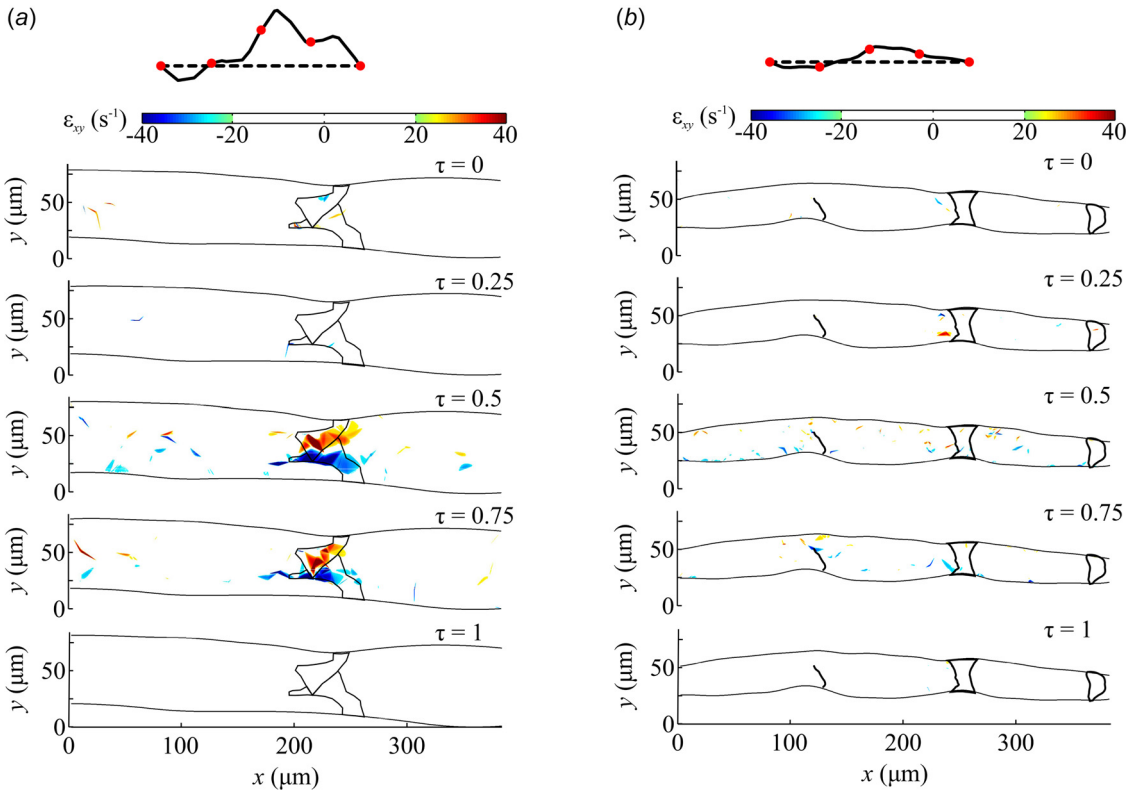

Fig. 9 The lymph shear strain field inside lymphatic vessels, distal from the inguinal lymph node, for the (*a*) normal and (*b*) affected mice at five separate points in a mean velocity cycle, $\tau = 0$, 0.25, 0.5, 0.75, and 1.0. The wall and outline of the valves are shown. The flow waveform is shown with red circles denoting the five different time points.

field of view included only three neighboring lymphangions, it is expected that temporary lymph pressure changes outside of the field of view occurred in other lymphangions distally and/or proximally. Temporary changes in lymph pressure due to skeletal muscle movement or any other external force that can inhibit lymph flow temporarily can raise the pressure locally and may result in retrograde lymph flow.

One of the responses of ECs to fluid flow is the upregulation of endothelial nitric oxide synthase and sequential release of nitric oxide (NO), which promotes smooth muscle cell relaxation [33,34]. Regional lymphatic variations of NO concentration have been previously observed in vivo, in vitro, and in silico [34–36]. Potentially, the lymphangion regional variation of NO may be playing a role in the lack of contractility uniformity observed in our studies where the center of the lymphangions tend to contract most, although the diameter changes are heterogeneous (Fig. 3). It is important to consider that the regions coinciding with lymphatic valves lack smooth muscle cells, and adjacent to this site NO tends to be present at higher concentrations [36,37].

The previously observed local accumulation of NO adjacent to the lymphatic valves may be explained by the pathlines in the flow field and increased particle residence times inside the recirculation zones and valvular sinus regions. The combination of physiological Reynolds number and intraluminal lymphatic valve anatomy promotes lymph flow separation and formation of recirculation zones, as highlighted by our studies. Our measurements showed that flow velocity inside the recirculation zones is predominantly about 0 μm/s, but with occasional increases in velocity that can reach up to 88 and 24 μm/s for the normal and affected mice, respectively, concomitant with vessel contractions (data not shown). The low velocities allow for molecules and cells to interact with the endothelium for extended periods of time, especially in the valvular sinus region where lymph flow is nearly stagnant (Figs. 10(*a*), 10(*b*), and 11). It is expected that the recirculation

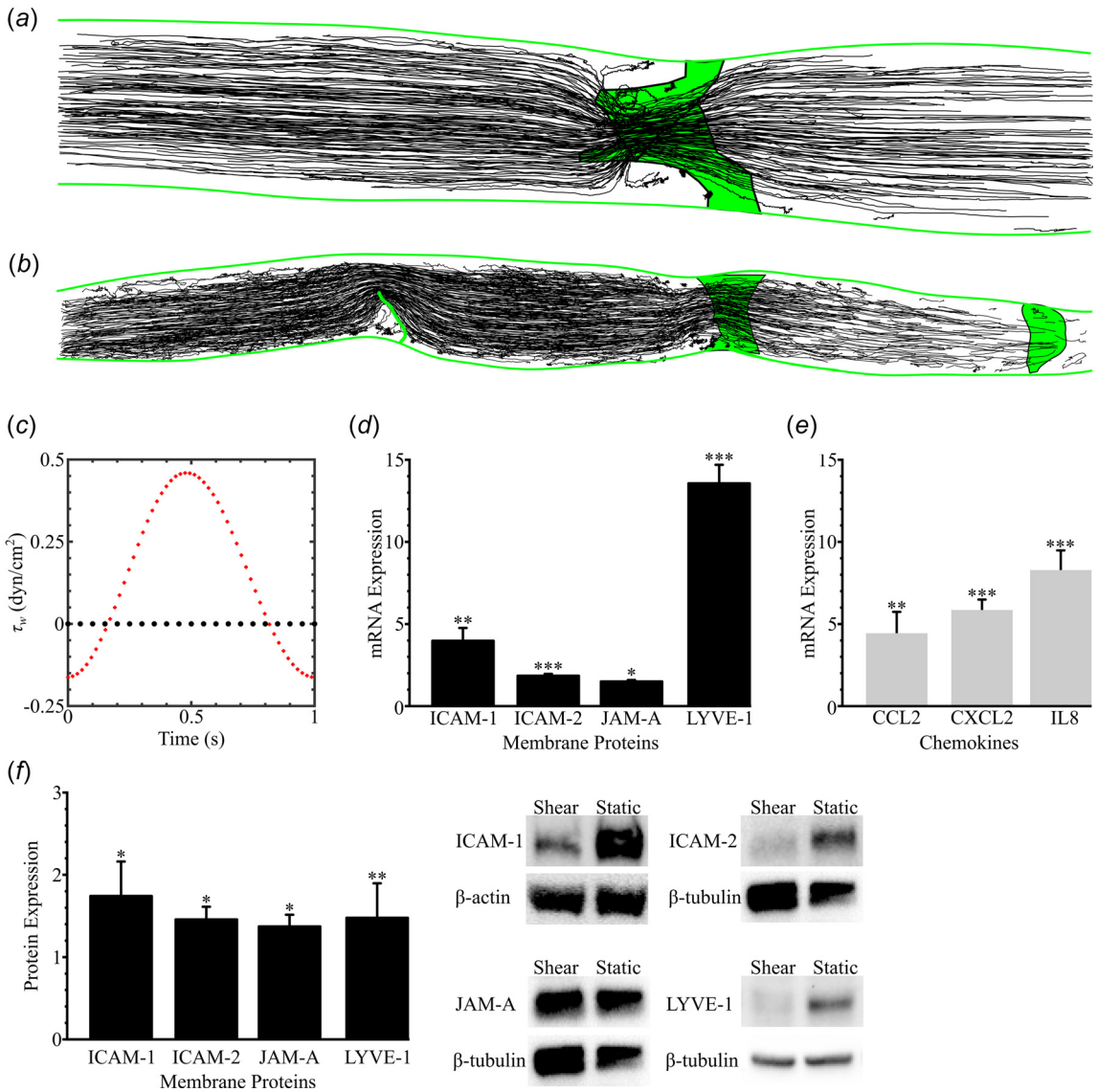

Fig. 10 Pathlines corresponding to the trajectory of fluorescent particle for 22.5 s in the lymphatic vessels of the (*a*) normal and (*b*) affected mice. The pathlines were used to generate representative flow condition waveforms. LECs were exposed in vitro to (*c*) pulsatile ML (+ + +) or static lymphatic sinus (○ ○ ○) representative flow conditions. In vitro LEC (*d*) ICAM-1, ICAM-2, JAM-A, LYVE-1 and (*e*) CCL2, CXCL2, and IL8 mRNA expression of static lymphatic sinus condition normalized by pulsatile ML waveform ($n = 7$, ANOVA, *$P < 0.05$, **$P < 0.01$, ***$P < 0.001$). In vitro LEC (*f*) ICAM-1, ICAM-2, JAM-A, LYVE-1 protein expression of static lymphatic VS condition normalized by pulsatile ML waveform ($n \geq 4$, ANOVA, *$P < 0.05$, **$P < 0.01$).

zones and valvular sinus regions contribute to a heterogeneous composition of lymph in the lymphangions with greater concentration of solutes, cytokines, and other molecules involved in cell signaling inside these near stagnant regions (Fig. 11).

The lymphatic endothelium coinciding with the recirculation zone experiences WSS magnitudes less than 1 dyn/cm^2 and an oscillatory shear index of 0.46, while the valvular sinus region flow near the valve origin is nearly stagnant. These WSS characteristics have been previously implicated in susceptibility to disease and an endothelial inflammatory phenotype in the cardiovascular system [38]. Fluid shear stress is known to regulate cardiovascular EC expression of cellular adhesion molecules that facilitate leukocyte binding, such as VCAM-1 and ICAM-1 [30,39–41]. ICAM-1 functions as a primary receptor for LFA-1, which is present on T cells, monocytes, neutrophils, dendritic cells, and macrophages. Dendritic cell expressed Mac-1 binds to ICAM-1 to mediate adhesion and transmigration, while blocking of ICAM-1 in LECs affects T cell adhesion, crawling, and transmigration [42,43]. Although ICAM-1 is generally considered to be the primary LFA-1 receptor in ECs, ICAM-2 also functions as a redundant receptor in lymphocyte trafficking and plays a role in neutrophil transmigration in blood endothelial cells [44,45]. Neutrophils express both LFA-1 and Mac-1, which facilitate adhesion to the endothelium [46]. LFA-1 and Mac-1 are each able to adhere to either to endothelial ICAM-1 or ICAM-2 [47,48]. The VS static conditions upregulated LEC ICAM-1 and ICAM-2, suggesting that LECs in the VS region will be primed toward a pro-inflammatory state. In circulatory system endothelial cells, the tight junction protein JAM-A has been shown to mediate extravasation via interaction with LFA-1 on leukocytes during diapedesis, while in LECs one study suggested that JAM-A plays a positive role in neutrophil transmigration [49–51]. Although the role of JAM-A in lymphatic endothelial transmigration has not been thoroughly examined, we observed that the VS static conditions upregulated LEC JAM-A expression, suggesting that transendothelial migration may be more favorable in this region (Figs. 10(*d*)–10(*f*) and 11). Similar results were observed for the major lymphatic hyaluronic acid (HA) receptor LYVE-1 that mediates leukocyte docking via interaction with HA as a surface glycocalyx. LYVE-1 HA interaction has been demonstrated to mediate lymphatic transendothelial migration of both dendritic cells and macrophages [52,53]. Although a LYVE-1 mediated mechanism has yet to be reported in the lymphatic transendothelial migration of lymphocytes, HA is also synthesized as a glycocalyx in T cells suggesting that T cells potentially engage in a similar transmigratory mechanism [54–56].

A potentially pro-inflammatory milieu generated by the flow field in the vicinity of lymphatic valves was also assessed by measuring the gene expression of transmigration relevant chemokines IL-8, CCL2, and CXCL2. IL-8 is a neutrophil attracting chemokine that regulates transendothelial migration and has been shown to be shear sensitive in human umbilical vein endothelial cells (HUVECs) [57–59]. The chemokine CXCL2 is another potent regulator of neutrophil transendothelial migration and its expression in HUVECs has also been shown to be shear sensitive [29,60]. Similarly, the expression of CCL2, a chemokine that recruits monocytes, T cells, and dendritic cells has been shown to be shear sensitive in HUVECS [61–64]. The static VS flow conditions upregulated the LEC mRNA expression of IL-8, CCL2, and CXCL2. Interestingly, both CXCL2 and IL-8 are preferentially expressed on the luminal rather than abluminal membrane facilitating luminal recruitment of leukocytes within the vessel [65]. A recent study has shown T cell extravasation into the surrounding tissue from murine lymphatic vessels [66]. Although this study

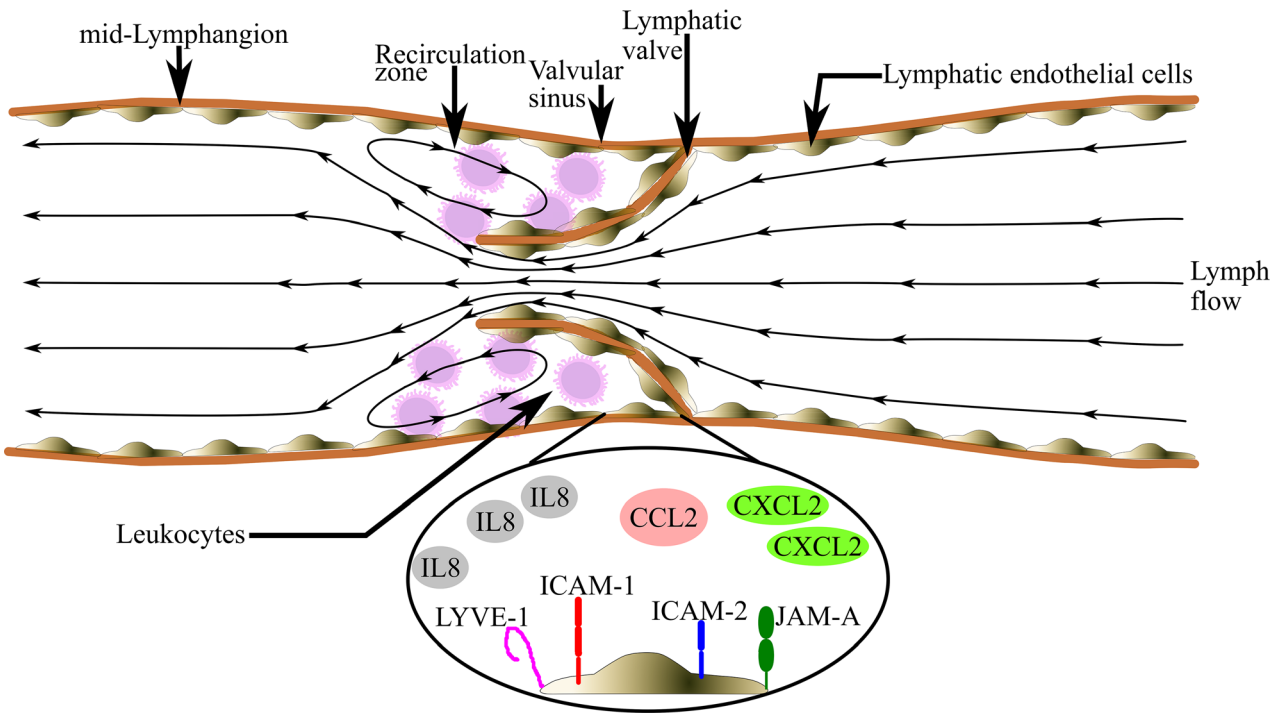

Fig. 11 Proposed lymphangion fluid flow model where the lymphatic valves introduce spatial fluid flow heterogeneity. Lymph accelerates as it approaches the lymphatic valve reaching a local maximum speed near the tip of the valve leaflets where the effective area is smallest. Lymph flow separates from the valve tips creating recirculation zones with long particle residence times. Lymph flow reattaches in the ML region and travels parallel to the wall. Near stagnant flow conditions persist in the VS region, especially in the vicinity of the lymphatic valve origin. The low wall shear stress conditions in the VS and recirculation zone serve to prime the LECs toward a pro-inflammatory phenotype by upregulating the expression of cellular adhesion molecules ICAM-1, ICAM-2, JAM-A, and LYVE-1 and secreted transmigration relevant chemokines IL-8, CCL2, and CXCL2. The long particle residence time in the VS region allows leukocytes to interact with a potentially primed pro-inflammatory lymphatic endothelium.

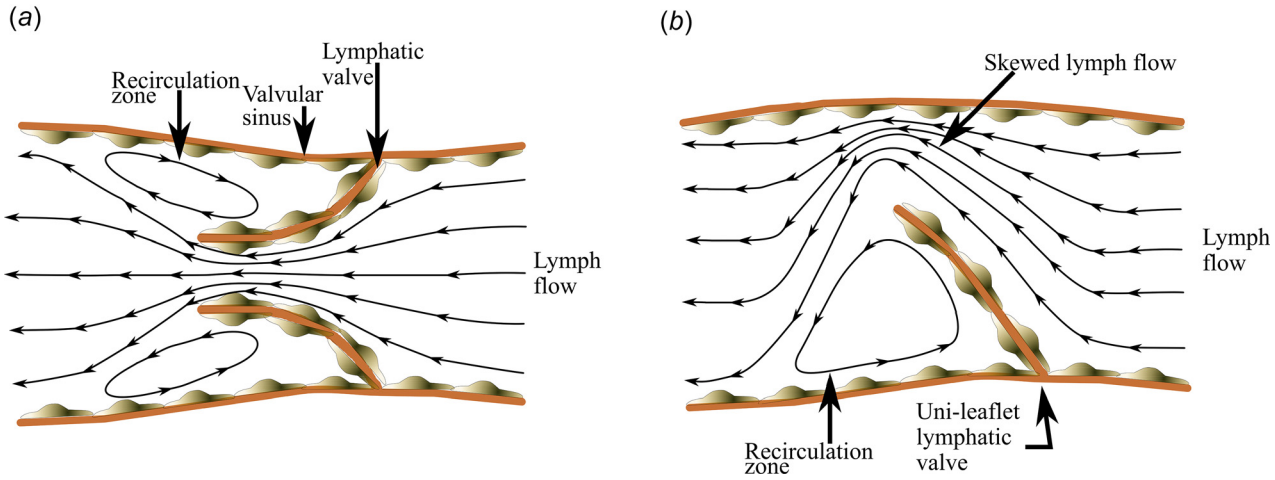

Fig. 12 Lymphatic flow field through a lymphangion with a (*a*) bileaflet valve displays a more symmetric flow field in contrast with a (*b*) unileaflet valve that skews higher velocity lymph flow toward the vessel wall and results in a much larger recirculation zone

observed leukocyte extravasation from initial lymphatics into the surrounding tissue, we propose that entrapment of leukocytes in the low shear stress near-stagnant environment of the valvular sinus along with potentially higher concentrations of secreted chemokines IL-8, CCL2, and CXCL2 and primed LECs with upregulated expression of cellular adhesion molecules ICAM-1, ICAM-2, JAM-A, and LYVE-1 creates conditions favorable for transendothelial migration (Fig. 11).

In the cardiovascular system, leukocytes are affected by shear stresses as low as 1–10 dyn/cm^2 [67]. Reduced shear stress induces pseudo-pod projection in leukocytes, increasing spreading of leukocytes over ECs, and thus potential transendothelial migration [68]. Therefore, leukocytes may undergo diapedesis at a higher rate in ECs adjacent to recirculation zones and near the valve origins in the valvular sinus, where fluid stress is lower than other regions of the vessel. Given that LECs are also sensitive to fluid flow [16], it is possible that recirculation zones and the valvular sinus regions in the lymphatic system are characterized by a pro-inflammatory endothelium interacting with lymphocytes. The long particle residence time and pro-inflammatory endothelial milieu allows for lymphocytes to interact for extended periods and may facilitate transmigration. However, this process is not expected to be exclusive for lymphocytes, but may be relevant to any other cell circulating in the lymphatic system, for example, circulating tumor cells, and have potential clinical effects on in-transit metastasis [69,70]. The model proposed in Fig. 11 is based on the in vitro results, which suggest the presence of an underlying pro-inflammatory lymphatic endothelial phenotype in the valvular sinus. Future studies are needed to determine if recirculation zone flow indeed mediates diapedesis of leukocytes or other cell types in the lymphatic system.

Fluid and particle transport are significantly affected by the anatomy of the lymphatic vessels and valves in each mouse. The lymphatic vessels of the mouse models studied are similar in that they contain bileaflet valves that generally accelerate flow parallel to the vessel wall (Fig. 6). However, the affected mouse contained a malformed unileaflet valve that skewed lymph flow toward the vessel wall endothelium generating a higher-pressure stagnation point (Fig. 12). Stagnation points have been previously shown to affect the morphology, migration, and density of ECs [71]. This may be because stagnation points create gradients of WSS and increase the total pressures experienced by ECs [71,72]. Vascular sites that coincide with stagnation points have also been shown to affect the adhesion of monocytes, as well as the functionality of endothelial gap junction proteins [72,73]. These combined effects may shift the lymphatic endothelium phenotype [71–75]. As a result, the ECs that line the vessel wall adjacent to the malformed valve are exposed to different forces and WSS profiles that may cause endothelial dysfunction with potential clinical consequences.

There is significant heterogeneity observed between the spatio-temporal velocity and strain profiles of the two animals studied, which likely results from interanimal anatomical variations. Shear and normal strain rates experienced by cells in lymph are dictated by advective acceleration as lymph travels through the converging valves. The normal and shear strains deform cells by compression or elongation and by shearing of the membrane, respectively. Membrane deformation can cause cytoskeletal and nuclear organization changes with potential changes in gene expression [76], and changes in leukocyte rolling behavior are associated with membrane deformation [77]. Shear strain rates have been shown to affect the viscosity of leukemic myeloblasts and lymphocytes [78], although not much is yet known about the relationship between strain and cells in lymphatic vessels. Along with strain and velocity, vorticity was heterogenous between the different mice, which is a consequence of inter- and intra-animal heterogeneity. The general trend of higher vorticity resulting at the core of the vessel was expected, as a shear layer forms at the lymphatic valves as flow travels through them. It is possible that increased vorticity induces greater rotation of lymphocytes and other contents in lymph, increasing the accessibility for interactions and biochemical reactions. In the case of the malformed valve, a shear layer is generated closer to the vessel wall, causing increased vorticity at the wall.

There were several experimental limitations inherent to the study of lymphatic flow in vivo. Although we corrected for in-plane motion due to breathing and muscle twitching, out-of-plane motions could not be corrected, limiting the length of time that could be studied. The presence of the intraluminal lymphatic valves introduces three-dimensionality into the fluid flow field, which is less common in low Reynolds number flows. Unfortunately, out-of-plane particle displacements could not be captured. in vivo experiments are paramount to better understand transport and physiology in the lymphatic system. However, anesthesia may affect lymph flow rates, although the effect may not be much different than changes that occur during sleep.

To the best of our knowledge, this is the first time that the local fluid flow properties of the lymphatic vessels distal from the inguinal lymph node have been characterized in vivo and connected to an LEC pro-inflammatory phenotype in vitro via upregulation of cellular adhesion molecules and secreted transmigration relevant chemokines. We quantified lymph flow using particle tracking of fluorescent microparticles in the lymphatic vessels of anesthetized mice. We compared the fluid flow properties between a vessel

with functioning bileaflet valves and an affected vessel that contained a malformed unileaflet valve along with bileaflet valves. We observed that normal bileaflet valves significantly affect the flow field by generating a relatively higher-momentum lymph stream at the core of the vessel compared to slow-moving recirculation zones in the valvular sinus region. In contrast, malformed unileaflet valves skew lymph flow toward the vessel wall endothelium causing greater energy losses and slower flow. This type of valve incompetency is less efficient in propelling lymph, potentially causing accumulation of lymph. These data suggest that a high number of incompetent valves could potentially lead to lymphedema. These studies have provided unique and detailed insight into lymphatic flow, with potential applications to a variety of diseases that affect lymph transport and drug delivery.

Acknowledgment

D.T.S. Conceived of the in vivo study, designed the in vivo study and conducted the in vivo experiments. A.P. analyzed and interpreted the in vivo data. A.F.S. participated in the in vivo data analysis and drafted the paper. K.C., D.T.N., and P.M. participated in the in vivo data analysis. J.D.H. Conceived of the in vitro study, conducted the in vitro studies and analysis, participated in in vivo and in vitro data analysis, and helped draft the paper. J.M.J. Conceived of the in vivo and in vitro studies, designed the study, participated in in vivo and in vitro data analyses, conducted the experiments, coordinated the study and helped draft the paper.

This work was supported by the National Heart, Lung, and Blood Institute (NHLBI) grants T32HL007439 (to D.T. Sweet) and K25 HL107617 (to J.M. Jiménez), and NSF grants CAREER CMMI1842308 (to J.M. Jiménez) and Graduate Research Fellowship Program S12100000000937 (to A.F. Smith). We thank Dr. Melissa D. Sánchez for constructive criticism.

Funding Data

- National Science Foundation (NSF) (Funder ID: 10.13039/100000001).

References

[1] Rusznyák, I., Földi, M., and Szabó, G., 1967, *Lymphatics and Lymph Circulation: Physiology and Pathology,* 2nd English ed., Oxford: Pergamon Press, Oxford, NY.

[2] Trzewik, J., Mallipattu, S. K., Artmann, G. M., Delano, F. A., and Schmid-Schonbein, G. W., 2001, "Evidence for a Second Valve System in Lymphatics: Endothelial Microvalves," Faseb J., **15**(10), pp. 1711–1717.

[3] Murfee, W. L., Rappleye, J. W., Ceballos, M., and Schmid-Schönbein, G. W., 2007, "Discontinuous Expression of Endothelial Cell Adhesion Molecules Along Initial Lymphatic Vessels in Mesentery: The Primary Valve Structure," Lymphat. Res. Biol, **5**(2), pp. 81–89.

[4] Schmid-Schönbein, G. W., 1990, "Microlymphatics and Lymph Flow," Physiol. Rev, **70**(4), pp. 987–1028.

[5] Gannon, B. J., and Carati, C. J., 2003, "Endothelial Distribution of the Membrane Water Channel Molecule Aquaporin-1: Implications for Tissue and Lymph Fluid Physiology?," Lymphat. Res. Biol, **1**(1), pp. 55–66.

[6] Leak, L. V., and Burke, J. F., 1966, "Fine Structure of the Lymphatic Capillary and the Adjoining Connective Tissue Area," Am. J. Anat., **118**(3), pp. 785–809.

[7] Fraley, E. E., and Weiss, L., 1961, "An Electron Microscopic Study of the Lymphatic Vessels in the Penile Skin of the Rat," Am. J. Anat., **109**(1), pp. 85–101.

[8] Jamalian, S., 2017, "Demonstration and Analysis of the Suction Effect for Pumping Lymph From Tissue Beds at Subatmospheric Pressure," Sci. Rep, **7**, p. 12080.

[9] Rasmussen, J. C., Tan, I.-C., Marshall, M. V., Adams, K. E., Kwon, S., Fife, C. E., Maus, E. A., Smith, L. A., Covington, K. R., and Sevick-Muraca, E. M.,. 2010, "Human Lymphatic Architecture and Dynamic Transport Imaged Using Near-Infrared Fluorescence," Transl. Oncol., **3**(6), pp. 362–367.

[10] Von Der Weid, P. Y., and Zawieja, D. C., 2004, "Lymphatic Smooth Muscle: The Motor Unit of Lymph Drainage," Int. J. Biochem. Cell Biol., **36**(7), pp. 1147–1153.

[11] Zawieja, D. C., von der Weid, P.-Y., and Gashev, A. A., 2008, *Microlymphatic Biology*, Microcirculation, Elsevier, Cambridge, MA, pp. 125–158.

[12] Dixon, J. B., Greiner, S. T., Gashev, A. A., Cote, G. L., Moore, J. E., and Zawieja, D. C.,. 2006, "Lymph Flow, Shear Stress, and Lymphocyte Velocity in Rat Mesenteric Prenodal Lymphatics," Microcirculation, **13**(7), pp. 597–610.

[13] Chong, C., Scholkmann, F., Bachmann S., Luciani, P., Leroux, J-C., Detmar, M., and Proulx. S., 2016, "In Vivo Visualization and Quantification of Collecting Lymphatic Vessel Contractility Using Near-Infrared Imaging," Sci. Rep., **6**, pp. 1–12.

[14] Breslin, J. W., and Kurtz, K. M., 2009, "Lymphatic Endothelial Cells Adapt Their Barrier Function in Response to Changes in Shear Stress," Lymphat. Res. Biol, **7**(4), pp. 229–237.

[15] Sabine, A., Bovay, E., Demir, C. S., Kimura, W., Jaquet, M., Agalarov, Y., Zangger, N., Scallan, J. P., Graber, W., Gulpinar, E., Kwak, B. R., Mäkinen, T., Martinez-Corral, I., Ortega, S., Delorenzi, M., Kiefer, F., Davis, M. J., Djonov, V., Miura, N., and Petrova, T. V.,. 2015, "FOXC2 and Fluid Shear Stress Stabilize Postnatal Lymphatic Vasculature," J. Clin. Invest, **125**(10), pp. 3861–3877.

[16] Sweet, D. T., Jiménez, J. M., Chang, J., Hess, P. R., Mericko-Ishizuka, P., Fu, J., Xia, L., Davies, P. F., and Kahn, M. L.,. 2015, "Lymph Flow Regulates Collecting Lymphatic Vessel Maturation In Vivo," J. Clin. Invest., **125**(8), pp. 2995–3007.

[17] Yao, L., Pan, J., Setiadi, H., Patel, K. D., and McEver, R. P., 1996, "Interleukin 4 or Oncostatin M Induces a Prolonged Increase in P-Selectin mRNA and Protein in Human Endothelial Cells," J. Exp. Med., **184**(1), pp. 81–92.

[18] Pan, J., Xia, L., Yao, L., and McEver, R. P., 1998, "Tumor Necrosis Factor-α- or Lipopolysaccharide-Induced Expression of the Murine P-Selectin Gene in Endothelial Cells Involves Novel κB Sites and a Variant Activating Transcription Factor/cAMP Response Element," J. Biol. Chem., **273**(16), pp. 10068–10077.

[19] Woltmann, G., McNulty, C. A., Dewson, G., Symon, F. A., and Wardlaw, A. J., 2000, "Interleukin-13 Induces PSGL-1/P–Selectin–Dependent Adhesion of Eosinophils, but Not Neutrophils, to Human Umbilical Vein Endothelial Cells Under Flow," Blood, **95**(10), pp. 3146–3152.

[20] Johnson, L. A., Clasper, S., Holt, A. P., Lalor, P. F., Baban, D., and Jackson, D. G., 2006, "An Inflammation-Induced Mechanism for Leukocyte Transmigration Across Lymphatic Vessel Endothelium," J. Exp. Med., **203**(12), pp. 2763–2777.

[21] Lund, A. W., Medler, T. R., Leachman, S. A., and Coussens, L. M., 2016, "Lymphatic Vessels, Inflammation, and Immunity in Skin Cancer," Cancer Discovery, **6**(1), pp. 22–35.

[22] Choi, I., Chung, H. K., Ramu, S., Lee, H. N., Kim, K. E., Lee, S., Yoo, J., Choi, D., Lee, Y. S., Aguilar, B., and Hong, Y.-K., 2011, "Visualization of Lymphatic Vessels by Prox1-Promoter Directed GFP Reporter in a Bacterial Artificial Chromosome-Based Transgenic Mouse," Blood, **117**(1), pp. 362–365.

[23] von der Weid, P.-Y., Rahman, M., Imtiaz, M. S., and van Helden, D. F., 2008, "Spontaneous Transient Depolarizations in Lymphatic Vessels of the guinea Pig Mesentery: Pharmacology and Implication for Spontaneous Contractility," Am. J. Physiol. Circ. Physiol., **295**(5), pp. H1989–H2000.

[24] Atchison, D. J., and Johnston, M. G., 1997, "Role of Extra- and Intracellular Ca2+ in the Lymphatic Myogenic Response," Am. J. Physiol. Integr. Comp. Physiol., **272**(1), pp. R326–R333.

[25] Beckett, E. A. H., Hollywood, M. A., Thornbury, K. D., and McHale, N. G., 2007, "Spontaneous Electrical Activity in Sheep Mesenteric Lymphatics," Lymphat. Res. Biol., **5**(1), pp. 29–44.

[26] He, X., and Ku, D. N., 1996, "Pulsatile Flow in the Human Left Coronary Artery Bifurcation: Average Conditions," ASME J. Biomech. Eng., **118**(1), pp. 74–82.

[27] Jiménez, J. M., Prasad, V., Yu, M. D., Kampmeyer, C. P., Kaakour, A.-H., Wang, P.-J., Maloney, S. F., Wright, N., Johnston, I., Jiang, Y.-Z., and Davies, P. F.,. 2014, "Macro- and Microscale Variables Regulate Stent Haemodynamics, Fibrin Deposition and Thrombomodulin Expression," J. R. Soc. Interface, **11**(94), p. 20131079.

[28] Kato, H., Uchimura, I., Nawa, C., Kawakami, A., and Numano, F., 2001, "Fluid Shear Stress Suppresses Interleukin 8 Production by Vascular Endothelial Cells," Biorheology, **38**(4), pp. 347–353.

[29] Shaik, S. S., Soltau, T. D., Chaturvedi, G., Totapally, B., Hagood, J. S., Andrews, W. W., Athar, M., Voitenok, N. N., Killingsworth, C. R., Patel, R. P., Fallon, M. B., and Maheshwari, A., 2009, "Low Intensity Shear Stress Increases Endothelial ELR+ CXC Chemokine Production Via a Focal Adhesion Kinase-p38β MAPK-NF-κB Pathway," J. Biol. Chem., **284**(9), pp. 5945–5955.

[30] Chiu, J., Lee, P., Chen, C., Lee, C., Chang, S., Chen, L., Lien, S., Ko, Y., Usami, S., and Chien, S., 2004, "Shear Stress Increases ICAM-1 and Decreases VCAM-1 and E-Selectin Expressions Induced by Tumor Necrosis Factor-α in Endothelial Cells," Arterioscler. Thromb. Vasc. Biol., **24**(1), pp. 73–79.

[31] Lee, E. S., Boldo, L. S., Fernandez, B. O., Feelisch, M., and Harmsen, M. C., 2017, "Suppression of TAK1 Pathway by Shear Stress Counteracts the Inflammatory Endothelial Cell Phenotype Induced by Oxidative Stress and TGF-β1," Sci. Rep., **7**, p. 42487.

[32] Scholz, D., Ito, W., Fleming, I., Deindl, E., Sauer, A., Wiesnet, M., Busse, R., Schaper, J., and Schaper, W., 2000, "Ultrastructure and Molecular Histology of Rabbit Hind-Limb Collateral Artery Growth (Arteriogenesis)," Virchows Arch., **436**(3), pp. 257–270.

[33] Shirasawa, Y., Ikomi, F., and Ohhashi, T., 2000, "Physiological Roles of Endogenous Nitric Oxide in Lymphatic Pump Activity of Rat Mesentery In Vivo," Am. J. Physiol. Gastrointest. Liver Physiol., **278**(4), pp. G551–G556.

[34] Bohlen, H. G., Wang, W., Gashev, A., Gasheva, O., and Zawieja, D., 2009, "Phasic Contractions of Rat Mesenteric Lymphatics Increase Basal and Phasic Nitric Oxide Generation In Vivo," Am. J. Physiol. Heart Circ. Physiol., **297**(4), pp. H1319–HI328.

[35] Wilson, J. T., Wang, W., Hellerstedt, A. H., Zawieja, D. C., and Moore, J. E., 2013, "Confocal Image-Based Computational Modeling of Nitric Oxide Transport in a Rat Mesenteric Lymphatic Vessel," ASME J. Biomech. Eng., **135**(5), p. 051005.

[36] Bohlen, H. G., Gasheva, O. Y., and Zawieja, D. C., 2011, "Nitric Oxide Formation by Lymphatic Bulb and Valves is a Major Regulatory Component of Lymphatic Pumping," Am. J. Physiol. Circ. Physiol., **301**(5), pp. H1897–H1906.
[37] Bridenbaugh, E. A., Nizamutdinova, I. T., Jupiter, D., Nagai, T., Thangaswamy, S., Chatterjee, V., and Gashev, A. A., 2013, "Lymphatic Muscle Cells in Rat Mesenteric Lymphatic Vessels of Various Ages," Lymphat. Res. Biol., **11**(1), pp. 35–42.
[38] Jiang, Y.-Z., Jiménez, J. M., Ou, K., McCormick, M. E., Zhang, L.-D., and Davies, P. F., 2014, "Hemodynamic Disturbed Flow Induces Differential DNA Methylation of Endothelial Kruppel-Like Factor 4 Promoter In Vitro and In Vivo," Circ. Res., **115**(1), pp. 32–43.
[39] Sampath, R., Kukielka, G. L., Smith, C. W., Eskin, S. G., and McIntire, L. V., 1995, "Shear Stress-Mediated Changes in the Expression of Leukocyte Adhesion Receptors on Human Umbilical Vein Endothelial Cells In Vitro," Ann. Biomed. Eng., **23**(3), pp. 247–256.
[40] Rosette, C., Roth, R. B., Oeth, P., Braun, A., Kammerer, S., Ekblom, J., and Denissenko, M. F., 2005, "Role of ICAM1 in Invasion of Human Breast Cancer Cells," Carcinogenesis, **26**(5), pp. 943–950.
[41] Nagel, T., Resnick, N., Atkinson, W. J., Dewey, C. F., and Gimbrone, M. A., 1994, "Shear Stress Selectively Upregulates Intercellular Adhesion Molecule-1 Expression in Cultured Human Vascular Endothelial Cells," J. Clin. Invest., **94**(2), pp. 885–889.
[42] Teijeira, A., Hunter, M. C., Russo, E., Proulx, S. T., Frei, T., Debes, G. F., Coles, M., Melero, I., Detmar, M., Rouzaut, A., and Halin, C., 2017, "T Cell Migration From Inflamed Skin to Draining Lymph Nodes Requires Intralymphatic Crawling Supported by ICAM-1/LFA-1 Interactions," Cell Rep., **18**(4), pp. 857–865.
[43] Muller, W. A., 2014, "How Endothelial Cells Regulate Transmigration of Leukocytes in the Inflammatory Response," Am. J. Pathol., **184**(4), pp. 886–896.
[44] Lehmann, J. C. U., Jablonski-Westrich, D., Haubold, U., Gutierrez-Ramos, J.-C., Springer, T., and Hamann, A., 2003, "Overlapping and Selective Roles of Endothelial Intercellular Adhesion Molecule-1 (ICAM-1) and ICAM-2 in Lymphocyte Trafficking," J. Immunol., **171**(5), pp. 2588–2593.
[45] Halai, K., Whiteford, J., Ma, B., Nourshargh, S., and Woodfin, A., 2014, "ICAM-2 Facilitates Luminal Interactions Between Neutrophils and Endothelial Cells In Vivo," J. Cell Sci., **127**(3), pp. 620–629.
[46] Schnoor, M., Alcaide, P., Voisin, M. B., and Van Buul, J. D., 2015, "Crossing the Vascular Wall: Common and Unique Mechanisms Exploited by Different Leukocyte Subsets During Extravasation," Mediators Inflamm., **2015**, pp. 1–23.
[47] Imhof, B. A., and Aurrand-Lions, M., 2004, "Adhesion Mechanisms Regulating the Migration of Monocytes," Nat. Rev. Immunol., **4**(6), pp. 432–444.
[48] Ley, K., Laudanna, C., Cybulsky, M. I., and Nourshargh, S., 2007, "Getting to the Site of Inflammation: The Leukocyte Adhesion Cascade Updated," Nat. Rev. Immunol., **7**(9), pp. 678–689.
[49] Ostermann, G., Weber, K. S. C., Zernecke, A., Schröder, A., and Weber, C., 2002, "JAM-I is a Ligand of the $\beta 2$ Integrin LFA-I Involved in Transendothelial Migration of Leukocytes," Nat. Immunol., **3**(2), pp. 151–158.
[50] Cera, M. R., Del Prete, A., Vecchi, A., Corada, M., Martin-Padura, I., Motoike, T., Tonetti, P., Bazzoni, G., Vermi, W., Gentili, F., Bernasconi, S., Sato, T. N., Mantovani, A., and Dejana, E., 2004, "Increased DC Trafficking to Lymph Nodes and Contact Hypersensitivity in Junctional Adhesion molecule-A—Deficient Mice," J. Clin. Invest., **114**(5), pp. 729–738.
[51] Ebnet, K., Suzuki, A., Ohno, S., and Vestweber, D., 2004, "Junctional Adhesion Molecules (JAMs): More Molecules With Dual Functions?," J. Cell Sci., **117**(1), pp. 19–29.
[52] Lawrance, W., Banerji, S., Day, A. J., Bhattacharjee, S., and Jackson, D. G., 2016, "Binding of Hyaluronan to the Native Lymphatic Vessel Endothelial Receptor LYVE-1 is Critically Dependent on Receptor Clustering and Hyaluronan Organization," J. Biol. Chem., **291**(15), pp. 8014–8030.
[53] Johnson, L. A., Banerji, S., Lawrance, W., Gileadi, U., Prota, G., Holder, K. A., Roshorm, Y. M., Hanke, T., Cerundolo, V., Gale, N. W., and Jackson, D. G., 2017, "Dendritic Cells Enter Lymph Vessels by Hyaluronan-Mediated Docking to the Endothelial Receptor LYVE-1," Nat. Immunol., **18**, pp. 762–770.
[54] Mahaffey, C. L., and Mummert, M. E., 2007, "Hyaluronan Synthesis is Required for IL-2-Mediated T Cell Proliferation," J. Immunol., **179**(12), pp. 8191–8199.
[55] Mummert, M. E., 2005, "Immunologic Roles of Hyaluronan," Immunol. Res., **31**(3), pp. 189–206.
[56] Mummert, M. E., Mummert, D., Edelbaum, D., Hui, F., Matsue, H., and Takashima, A., 2002, "Synthesis and Surface Expression of Hyaluronan by Dendritic Cells and Its Potential Role in Antigen Presentation," J. Immunol., **169**(8), pp. 4322–4431.
[57] Smart, S. J., and Casale, T. B., 1994, "TNF-α-Induced Transendothelial Neutrophil Migration is IL-8 Dependent," Am. J. Physiol.—Lung Cell. Mol. Physiol., **266**(3Pt.1), pp. L238–L245.
[58] Smith, W. B., Gamble, J. R., Clark-Lewis, I., and Vadas, M. A., 1993, "Chemotactic Desensitization of Neutrophils Demonstrates Interleukin-8 (IL-8)-Dependent and IL-8-Independent Mechanisms of Transmigration Through Cytokine-Activated Endothelium," Immunology, **78**(3), pp. 491–497.
[59] Cheng, M., 2007, "IL-8 Gene Induction by Low Shear Stress: Pharmacological Evaluation of the Role of Signaling Molecules," Biorheology, **44**(5–6), pp. 349–360.
[60] Zlotnik, A., and Yoshie, O., 2012, "The Chemokine Superfamily Revisited," Immunity, **36**(5), pp. 705–716.
[61] Huang, D., Wang, J., Kivisakk, P., Rollins, B. J., and Ransohoff, R. M., 2001, "Absence of Monocyte Chemoattractant Protein 1 in Mice Leads to Decreased Local Macrophage Recruitment and Antigen-Specific T Helper Cell Type 1 Immune Response in Experimental Autoimmune Encephalomyelitis," J. Exp. Med., **193**(6), pp. 713–726.
[62] Berman, J. W., Guida, M. P., Brosnan, C. F., Amat, J., and Warren, J., 1996, "Localization of Monocyte Chemoattractant Peptide-1 Expression in the Central Nervous System in Experimental Autoimmune Encephalomyelitis and Trauma in the Rat," J. Immunol., **156**(8), pp. 3017–3023.
[63] Dogan, R.-N. E., Elhofy, A., and Karpus, W. J., 2008, "Production of CCL2 by Central Nervous System Cells Regulates Development of Murine Experimental Autoimmune Encephalomyelitis Through the Recruitment of TNF- and iNOS-Expressing Macrophages and Myeloid Dendritic Cells," J. Immunol., **180**(11), pp. 7376–7384.
[64] Yu, H., Zeng, Y., Hu, J., and Li, C., 2002, "Fluid Shear Stress Induces the Secretion of Monocyte Chemoattractant Protein-1 in Cultured Human Umbilical Vein Endothelial Cells," Clin. Hemorheol. Microcirc., **26**(3), pp. 199–207.
[65] Rigby, D. A., Ferguson, D. J. P., Johnson, L. A., and Jackson, D. G., 2015, "Neutrophils Rapidly Transit Inflamed Lymphatic Vessel Endothelium Via Integrin-Dependent Proteolysis and Lipoxin-Induced Junctional Retraction," J. Leukoc. Biol., **98**(6), pp. 897–912.
[66] Hunter, M. C., Teijeira, A., Montecchi, R., Russo, E., Runge, P., Kiefer, F., and Halin, C., 2019, "Dendritic Cells and T Cells Interact Within Murine Afferent Lymphatic Capillaries," Front. Immunol., **10**, p. 520.
[67] Makino, A., Shin, H. Y., Komai, Y., Fukuda, S., Coughlin, M., Sugihara-Seki, M., and Schmid-Schönbein, G. W., 2007, "Mechanotransduction in Leukocyte Activation: A Review," Biorheology, **44**(4), pp. 221–249.
[68] Moazzam, F., DeLano, F. A., Zweifach, B. W., and Schmid-Schonbein, G. W., 1997, "The Leukocyte Response to Fluid Stress," Proc. Natl. Acad. Sci. U. S. A, **94**(10), pp. 5338–5343.
[69] Nathanson, S. D., 2003, "Insights Into the Mechanisms of Lymph Node Metastasis," Cancer, **98**(2), pp. 413–423.
[70] Roses, D. F., Harris, M. N., Rigel, D., Carrey, Z., Friedman, R., and Kopf, A. W., 1983, "Local and in-Transit Metastases Following Definitive Excision for Primary Cutaneous Malignant Melanoma," Ann. Surg., **198**(1), pp. 65–69.
[71] Szymanski, M. P., Metaxa, E., Meng, H., and Kolega, J., 2008, "Endothelial Cell Layer Subjected to Impinging Flow Mimicking the Apex of an Arterial Bifurcation," Ann. Biomed. Eng., **36**(10), pp. 1681–1689.
[72] Chiu, J.-J., Chen, C.-N., Lee, P.-L., Tsair Yang, C., Sheng Chuang, H., Chien, S., and Usami, S.,. 2003, "Analysis of the Effect of Disturbed Flow on Monocytic Adhesion to Endothelial Cells," J. Biomech., **36**(12), pp. 1883–1895.
[73] DePaola, N., Davies, P. F., Pritchard, W. F., Florez, L., Harbeck, N., and Polacek, D. C., 1999, "Spatial and Temporal Regulation of Gap Junction connexin43 in Vascular Endothelial Cells Exposed to Controlled Disturbed Flows In Vitro," Proc. Natl. Acad. Sci. U. S. A, **96**(6), pp. 3154–3159.
[74] Ostrowski, M. A., Huang, N. F., Walker, T. W., Verwijlen, T., Poplawski, C., Khoo, A. S., Cooke, J. P., Fuller, G. G., and Dunn, A. R.,. 2014, "Microvascular Endothelial Cells Migrate Upstream and Align Against the Shear Stress Field Created by Impinging Flow," Biophys. J., **106**(2), pp. 366–374.
[75] Arslan, N., Isik, S., and Uykan, O., 2010, "Steady and Disturbed Flow Effects on Human Umbilical Vein Endothelial Cells (HUVECs) in Vascular System: An Experimental Study," Acta Bioeng. Biomech., **12**(4), pp. 3–9.
[76] Jain, N., Iyer, K. V., Kumar, A., and Shivashankar, G. V., 2013, "Cell Geometric Constraints Induce Modular Gene-Expression Patterns Via Redistribution of HDAC3 Regulated by Actomyosin Contractility," Proc. Natl. Acad. Sci., **110**(28), pp. 11349–11354.
[77] Coghill, P. A., Kesselhuth, E. K., Shimp, E. A., Khismatullin, D. B., and Schmidtke, D. W., 2013, "Effects of Microfluidic Channel Geometry on Leukocyte Rolling Assays," Biomed. Microdev., **15**(1), pp. 183–193.
[78] Lichtman, M. A., 1973, "Rheology of Leukocytes, Leukocyte Suspensions, and Blood in Leukemia Possible Relationship to Clinical Manifestations," J. Clin. Invest., **52**(2), pp. 350–358.